



Pressure Distributions on a 0.02-Scale Space Shuttle Orbiter Nose at Mach 21.5 in Helium

George C. Ashby, Jr., Peter T. Bernot, and William C. Woods



Pressure Distributions on a 0.02-Scale Space Shuttle Orbiter Nose at Mach 21.5 in Helium

George C. Ashby, Jr., Peter T. Bernot, and William C. Woods
Langley Research Center • Hampton, Virginia

National Aeronautics and
Space Administration
Code JTT
Washington, D.C.
20546-0001

B U L K R A T E
POSTAGE & FEES PAID
NASA Permit No. G-27

Official Business
Penalty for Private Use, \$300

Postmaster: If undeliverable (Section 158 Postal Manual) Do Not Return



The use of trademarks or names of manufacturers in this report is for accurate reporting and does not constitute an official endorsement, either expressed or implied, of such products or manufacturers by the National Aeronautics and Space Administration.

Acknowledgments

The calculations and plots of the angles from the SEADS algorithm were provided by M. W. Henry of Analytical Mechanics Associates, Inc., Hampton, Virginia.

Summary

Pressure distributions on a 0.02-scale model of the Space Shuttle orbiter forward fuselage were obtained in the 22-inch aerodynamic leg of the Langley Hypersonic Helium Tunnel Facility (Helium Tunnel) at a nominal free-stream Mach number of 21.5, a ratio of specific heats of 1.67, and a unit Reynolds number of $13 \times 10^6 \text{ ft}^{-1}$ for inclusion in the database of the Shuttle entry air data system (SEADS). The data were measured at model angles of attack $\alpha = 0^\circ$ – 50° in 5° increments at sideslip $\beta = 0^\circ$ and at model $\beta = -5^\circ$ – 5° for $\alpha = 5^\circ, 20^\circ, 35^\circ$, and 40° .

These helium data at Mach 21.5 displayed trends similar to those obtained from tests at Mach 6 and 10 in air. Specifically noted is a shift of the location of the maximum pressure to a lower surface slope than predicted by modified Newtonian theory at $\alpha > 15^\circ$. However, this phenomenon did not occur in flight. Analysis of tests at Mach 6 in the Langley Hypersonic CF_4 Tunnel, which correspond to a lower ratio of specific heat in the postshock region than the data obtained in helium and air, showed a reduction of the stagnation point shift at the higher α . The difference between flight and wind tunnel pressure distributions is likely due to high-temperature gas chemistry effects in flight, which include lower effective specific heat ratios but which were not completely duplicated in the wind tunnels.

In addition, the SEADS air data algorithm, which is based on the ideal gas wind tunnel data to Mach 10, predicts the model α and β in the Helium Tunnel from the pressures of the current test within 1° and 0.5° , respectively, at $\alpha \approx 8^\circ$ to 45° . With the current data, the base for the flight algorithm is extended to a significantly higher Mach number.

Introduction

The Shuttle entry air data system (SEADS) is an experimental, subsonic-to-hypersonic means (ref. 1) for acquiring accurate air data parameters for the Space Shuttle orbiter as it descends from space to the ground. The system was installed on the Space Shuttle orbiter *Columbia* and flown first on Space Transportation System (STS) flight STS-61-C (ref. 2) and later on STS-28, STS-32, STS-35, and STS-40 as part of the NASA Space Shuttle orbiter experiment (OEX) program. The SEADS system consists of 20 pressure orifices. Fourteen orifices are arranged in a cruciform pattern and are installed in a Space Shuttle baseline-geometry nose cap assembly; the other six orifices are on the forward fuselage. Each orifice is connected to a low- and high-range transducer to cover the pressures of the flight envelope. The data

are stored on the OEX recording system for postflight analysis. (See ref. 3.) Extensive ground-based experiments and analyses based on modified Newtonian theory were performed to develop the preflight algorithm that enables researchers to convert the SEADS pressure distribution data to air data, vehicle α and β , and free-stream dynamic pressure q_∞ . (See ref. 1.)

This data reduction algorithm incorporated Newtonian pressure correction factors based on wind tunnel data. The preflight database contained information obtained across the range from subsonic to a Mach number of 10 on various scaled models of the orbiter nose (refs. 4–9); that database was then used to develop the correction factors. Subsequently, the correction factors were calibrated based on data from STS-61-C (ref. 2) and STS-35. Only data from those two flights were involved in the final pressure corrections because a particularly important forward fuselage orifice on the other SEADS flights (STS-28, STS-32, and STS-40) was not installed, which compromised the results. However, a high level of confidence can be placed in the flight data because of repeatability and the excellent agreement with other flight data sources—notably, the operational instrumentation and best-estimated trajectory in reference 2.

The purpose of this paper is to present and assess the quality of the data obtained in the 22-inch aerodynamic leg of the Langley Hypersonic Helium Tunnel Facility (Helium Tunnel) at a free-stream Mach number $M_\infty = 21.5$ and a specific heat ratio $\gamma = 1.67$ for incorporation into the SEADS database that had been limited to $M_\infty < 10$ in air and $\gamma = 1.4$. The tests in the Helium Tunnel had an average $M_\infty = 21.5$ and a unit Reynolds number $N_{Re} = 13 \times 10^6 \text{ ft}^{-1}$. Angle of attack α was varied from 0° to 50° in 5° increments at $\beta = 0^\circ$, and β was varied from -5° to 5° for $\alpha = 5^\circ, 20^\circ, 35^\circ$, and 40° . The model is the same one tested at $M_\infty = 6$ in air (ref. 4) and CF_4 as well as at $M_\infty = 10$ in air (ref. 5); it represents the forward fuselage region of the Space Shuttle orbiter extending back to the canopy region (full-scale station of 225 in.) and includes the forward reaction control system (RCS) jet ports. Thirty-six pressure orifices, including the SEADS and Development Flight Instrument (DFI) locations, were incorporated into the model.

Data are presented in tabular form; also, selected data are plotted to show significant trends and to provide comparisons with the other hypersonic wind tunnel data in air (refs. 4 and 5) and in CF_4 (unpublished). In addition, α and β values are calculated from the present pressure distributions based on the preflight algorithm of reference 1 and are

compared with the corresponding wind tunnel test values.

Symbols

C_{pi}	pressure coefficient, $\frac{p_i - p_\infty}{q_\infty}$
M_∞	free-stream Mach number
N_{Re}	unit Reynolds number, ft^{-1}
$p_{t,\infty}$	tunnel total pressure, psia
$p_{t,2}$	total pressure behind normal shock, psia
p_∞	tunnel free-stream static pressure, psia
q_∞	tunnel free-stream dynamic pressure, psia
$T_{t,\infty}$	tunnel total temperature, °F
x, y, z	model coordinate system (fig. 2), in.
α	angle of attack, deg
β	angle of sideslip, deg
γ	ratio of specific heats
η_i	surface slope at orifice relative to Z-axis in the X-Z plane (fig. 2), deg
λ_i	surface slope at orifice relative to Y-axis in the X-Y plane (fig. 2), deg
ϕ_i	roll angle of orifice relative to Y-axis in the Y-Z plane (fig. 2), deg

Apparatus, Model, and Tests

Tunnel

The pressure distributions were obtained in the 22-inch aerodynamic leg of the Helium Tunnel. The facility utilizes a contoured axisymmetric nozzle and operates at a nominal $M_\infty = 20$. Calibration surveys presented in reference 10 indicate the test section $M_\infty = 17.5$ to 22.2 at a tunnel total pressure $p_{t,\infty} = 200$ to 3000 psia, respectively. At $p_{t,\infty} = 2000$ psia, the test section averaged $M_\infty = 21.5$ with a random variation across the test core as high as 0.5. The 0.5 variation occurs on the centerline and is negative (i.e., corresponds to an increase in the total pressure behind a normal shock $p_{t,2}$ at the centerline). Similarly, the flow angularity is usually less than 0.4°. (See ref. 10.)

The Helium Tunnel is operated primarily at ambient tunnel total temperature $T_{t,\infty}$ because helium does not require heat to avoid liquefaction at these flow conditions. This facility operates in the blow-down mode and the average test run is about 30 sec. After each run, the helium is reclaimed, purified, and stored in high-pressure tanks for reuse.

Model

The 0.02-scale test model, fabricated from stainless steel, represents the forward fuselage region of the Space Shuttle orbiter including the RCS jet ports. In figure 1 are photographs of the model and of the four stings that alleviate flow blockage problems at high α 's and that keep the model in the core of the flow. The stings employed canted model-mounting plates in which the angular offsets were 15°, 30°, and 45° relative to the X-axis in the X-Z plane. Thirty-six pressure orifices with 0.020-in-internal-diameter tubes were installed in the model. The pressure tubes were successively jumped within about 12 in. to an inside diameter of 0.060 in. to bring the pressure-settling time to the tunnel-operating time. The model coordinate system is shown in figure 2 and the orifice numbers and locations, which were accurately measured after model fabrication, are presented in table I. The model was machined within ± 0.005 in. of the specified aerolines, and orifice locations were within ± 3.0 percent of those specified. A front-view sketch of the model shows the relative locations of all orifices. (See fig. 3.) The SEADS array of orifices is represented by orifices 1 to 20; the remaining 16 orifices duplicate the DFI pressure ports on the full-scale orbiter and are correspondingly numbered.

Instrumentation

Model pressures were measured by multirange Baratron (MKS Instruments Inc., Andover, MA) and Barocel (Barocel Datametries, Wilmington, MA) transducers and recorded continuously at 20 samples per sec for the full run. The values were selected near the end of the run when they became constant. The measurements are believed accurate to ± 1 percent of the reading based on reference pressure runs conducted daily before tunnel operation and on the repeatability of the pressures near the stagnation point in repeat runs. In a reference pressure run, a series of known pressures are applied to the transducers based on a working standard, and the output readings are checked to ensure transducer integrity and to verify the calibration constants. The pressures near the stagnation point were found to repeat to ± 1 percent for runs at the same α and β but with the model nose in different locations in the tunnel test core.

These repeat runs were performed when the model was pitched through α in the vertical plane at $\beta = 0^\circ$, then was rotated 90° and pitched in the vertical plane for β at fixed α 's. The model α , β , and roll were set with a cathetometer and an inclinometer in conjunction with the model baseplate and sting surfaces that had been aligned before installation in the tunnel. While the model was illuminated by an electron beam to show the flow field, photographs were obtained and are presented in figure 4 for $\alpha = 5^\circ$ to 50° . These photographs were useful in establishing that the flow about the model is smooth and free of any appearance of flow blockage for the present α range. Details of the electron beam theory and system are presented in reference 11.

Test Conditions and Methods

The Helium Tunnel tests were conducted at a nominal $p_{t,\infty} = 2000$ psia and $T_{t,\infty} = 35^\circ$ to 75°F ; the average $M_\infty = 21.5$ and $N_{Re} = 13 \times 10^6 \text{ ft}^{-1}$. Because M_∞ varied within the test core and the model nose location in the test section also varied with each run, the maximum pressure on the model face, determined from fairings of the pressures in that region, was used in conjunction with measured $p_{t,\infty}$ and $T_{t,\infty}$ to determine M_∞ for the individual runs (generally, flow conditions are inferred from previous calibration tests with a pitot pressure rake). Tunnel parameters determined from the local M_∞ along with the model attitudes are listed in table II in which the free-stream dynamic pressure q_∞ , free-stream static pressure p_∞ , and $p_{t,2}$ were corrected for intermolecular force effects based on the method presented in reference 12.

Angle of attack was varied from 0° to 50° in 5° increments at $\beta = 0^\circ$ and β was varied from -5° to 5° at $\alpha = 5^\circ, 20^\circ, 35^\circ$, and 40° . For the varying α tests, the model was pitched in the tunnel vertical plane at $\beta = 0^\circ$; for the varying β tests, the model was rotated $\pm 90^\circ$ and sideslipped in the vertical plane at fixed α . With respect to the Mach number in the core, the model at the lower α 's is nearest the nozzle centerline and thus undergoes the largest variation from the average; that variation can be as much as 0.5. The model in all circumstances is in a gradient of at least ± 0.1 . Except near the centerline of the tunnel at the low α , the data from the stagnation region of the model do not appear to be strongly affected by the gradient.

Results and Discussion

Presentation of Results

A complete tabulation of orifice pressures, expressed as C_{pi} , is presented in table III for $\alpha = 0^\circ$ to

50° at $\beta = 0^\circ$. Tables IV through VII list the values obtained at $\beta = -5^\circ$ to 5° for $\alpha = 5^\circ, 20^\circ, 35^\circ$, and 40° . Selected data from the current test and from the other wind tunnel tests (refs. 4 and 5) are presented in figures 5–10 and analyzed in the subsequent discussion.

Pitch Plane

According to the modified Newtonian impact theory on which the SEADS algorithm is based (ref. 1), the maximum pressure on the model nose would be expected at the point where the surface slope is greatest relative to the flow (usually 90° , $\eta_i = 0^\circ$ for this study) and is referred to herein as the Newtonian location. To determine the actual locations of maximum pressure in the pitch (X - Z) plane, the pressure distribution on the nose in the plane of symmetry was plotted versus surface slope for the vertical Z -axis of the model at each α (fig. 5); note that η_i decreases from left to right. Also presented in figure 5 are the wind tunnel results at $M_\infty = 6$ in air (ref. 4) and CF_4 (unpublished) and at $M_\infty = 10$ in air. (See ref. 5.) Note that the ordinate scales have been shifted equal amounts to show the individual pressure values clearly and the peak locations as indicated by the data fairings. The curves were fitted by the method of least squares and the maximum point was determined from the first derivative, thereby allowing the relative differences between the actual (solid) and the Newtonian locations (dashed) to be readily determined. Beyond $\alpha \approx 10^\circ$ at all three Mach numbers and in all test media, the peak pressures occur at larger values of η_i than the Newtonian location indicates. Thus, the peak pressure occurs at a surface slope less than 90° to the flow ($\eta_i > 0^\circ$) for $\alpha > 10^\circ$. (See fig. 2.)

To show the relative differences in slope between Newtonian and measured maximum pressure locations and to compare the differences at the three Mach numbers, the values are plotted in figure 6. Because maximum pressure locations in terms of η_i are directly related to the model α , they are so plotted in the figure. If the surface slopes for maximum pressure agreed with the Newtonian locations, the test values would lie along the 45° diagonal. However, agreement occurs only at $\alpha < 15^\circ$. For $\alpha > 15^\circ$, the surface slope for maximum pressure location is as much as 5° to 8° higher than α (i.e., a lower surface slope relative to the flow) and is apparently independent of test medium and M_∞ .

The data at $M_\infty = 6$ in CF_4 show that the deviation in the stagnation point locations in those tests is delayed until about $\alpha = 20^\circ$; at that point and to $\alpha = 30^\circ$, the deviation shifts as much as it did in air,

then drops continuously to about half the air deviation beyond that angle. Tests in CF_4 are meant to simulate the inviscid portion of the stagnation region in flight by providing a higher normal shock density ratio (lower value of γ ; approximately 1.1 as opposed to 1.4 for air) in the postshock region; thus, the differences between the stagnation points in a perfect gas, air, and CF_4 indicate a γ effect. This observation is reinforced by the results of reference 13, which reports the pressure tests of a 0.025-scale model of the Space Shuttle orbiter nose in the Langley Expansion Tube at hypersonic and hypervelocity conditions with air, helium, and CO_2 as test gases and shows a similar inverse shift of the maximum pressure location at $\alpha = 32^\circ$ with effective γ , which varied from 1.1 to 1.67 in the tests.

When the flight data were examined, no shift of the stagnation point off the Newtonian location was evident (ref. 2); therefore, the high-temperature gas chemistry effects in the stagnation region in flight, which include a reduced effective γ , combined to eliminate the shift. However, the flow phenomenon that causes the shift in the location of the maximum pressure in the wind tunnel tests is not completely understood because it appears to be related to the geometry of the configuration as well as to γ . For example, this same type of deviation between the faired and Newtonian locations of the maximum pressure was observed at $M_\infty = 6$ in air for a two-dimensional parabolic body with a 90° surface slope (to the flow) at its nose (ref. 14), but it did not occur for the same contour as a body of revolution (ref. 15), nor for a two-dimensional circular arc body (also in ref. 14). The maximum pressure locations for the parabolic bodies are also plotted in figure 6. The body-of-revolution values lie on the diagonal, but for the two-dimensional parabolic body, the deviation from the Newtonian location begins as α increases from 0° . The locations of the peak pressures for the Space Shuttle model are found to deviate from modified Newtonian theory for $\alpha > 15^\circ$ and to agree with the results from reference 14 for a two-dimensional parabolic body at $\alpha = 20^\circ$ and 25° . This dichotomy in the movement of the stagnation point with α between models within a similar class in a hypersonic wind tunnel and of the Space Shuttle nose in the same wind tunnel and in flight shows that wind tunnel pressure data for flight prediction must be approached cautiously and verified in flight.

To determine how well the data at $M_\infty = 21.5$ in helium correlate with the SEADS flight-angle determination method, the original preflight algorithm was used to calculate model α 's for the wind tunnel test from the pressure data of that test. The

flight algorithm was established based on the design values of the orifice locations and surface slopes. The as-constructed values of the full-scale SEADS were within 2 to 3 percent of design based on actual measurements, and analysis showed no significant effects of this level of variation on the air data calculations. The calculated model α 's with the algorithm are shown in figure 7. Excellent agreement occurs for $\alpha < 20^\circ$; for $\alpha > 20^\circ$, the maximum overprediction by the SEADS algorithm within its design range ($\alpha = 8^\circ$ to 45°) is about 1° at $\alpha = 45^\circ$. The SEADS requirement for an accuracy of $\pm 0.5^\circ$ dictated the derivation of the previously discussed pressure corrections.

Sideslip Plane

To determine the location of the maximum pressure on the model nose as it is deflected in the β (X - Y) plane, the pressure distributions on the nose in that plane were plotted versus the surface slope λ_i relative to the Y -axis at each orifice for $\alpha = 5^\circ, 20^\circ, 35^\circ$, and 40° and $\beta = -5^\circ$ to 5° . Figure 8 presents the results at $M_\infty = 21.5$ with the origins of the ordinate scales shifted to discriminate among the individual pressure peak locations and the relative differences between the faired and Newtonian locations. Because $\beta < 15^\circ$ at which the location of maximum pressure was observed to deviate from the Newtonian location in the pitch plane, the curves were expected to pass through the Newtonian location; the least-squares fit, along with the maximum point calculation, showed that the curves indeed do pass through. With only a few exceptions, the fairings are smooth through the points. The only exceptions occur at $\alpha = 5^\circ$ (fig. 8(a)), where the center of some points is slightly off the curves.

To determine the magnitude of the difference in β and the surface slope at which the pressures are equal, pressure coefficients for pairs of orifices that are equidistant from the nose centerline and have nearly the same surface slope (but are of opposite sign) are plotted in figure 9 versus β for $\alpha = 5^\circ, 20^\circ, 35^\circ$, and 40° . The curves for the pairs of orifices are presented in the order of their distance from the centerline; thus, the order of the absolute values of λ_i is relative to the Y -axis in the X - Y plane. The surface slope for each orifice is shown in the figure. The location at which the faired curves for the orifice pairs cross is the point where the pressures are the same (nulled) and β at which this occurs should be close to half the difference in slope between the two orifices. In general, β for equal pressures (null) has the same sign as the slope difference between the orifice pairs, and the two angles agree within 0.25°

to 0.5° . However, the differences are less consistent at $\alpha = 5^\circ$ than at the other α 's observed in figure 8. The pressure variations with β are close to linear for all orifice pairs at $\alpha > 5^\circ$, but the variations are nonlinear at $\alpha = 5^\circ$ for all orifice pairs with slopes relative to the Y-axis at $\lambda_i < 50^\circ$. (Compare figs. 9(a)–(c) with figs. 9(d)–(g).)

This performance at $\alpha = 5^\circ$ also occurs when the optimized algorithm for SEADS is applied to the pressure data to calculate β . In figure 10 is a comparison between the angles calculated with the SEADS preflight algorithm and those of the present tests. Perfect agreement occurs along the 45° diagonal and all the data are within 0.5° except for the case of $\alpha = 5^\circ$, which varies by as much as 0.75° . This difference at the lowest α is attributed primarily to the M_∞ variation in the core near the tunnel centerline.

Concluding Remarks

Pressure distributions on a 0.02-scale model of the Space Shuttle orbiter forward fuselage were obtained in the 22-inch aerodynamic leg of the Langley Hypersonic Helium Tunnel Facility at a nominal free-stream Mach number of 21.5 and a ratio of specific heats of 1.67 for inclusion in the database of the Shuttle entry air data system. The data were measured at model angles of attack of 0° to 50° in 5° increments for 0° sideslip and at model sideslip angles of -5° to 5° for angles of attack of 5° , 20° , 35° , and 40° .

The helium data at a Mach number of 21.5 were found to display the same trends as those from similar tests at Mach 6 and 10 in air, which included a shift in the location of the maximum pressure to a lower surface slope than predicted by Newtonian theory at angles of attack above about 15° ; however, this effect did not occur in flight. By comparison, the data obtained at Mach 6 in the Langley Hypersonic CF_4 Tunnel, corresponding to a lower ratio of specific heats in the postshock region than those in helium and air, showed some reduction of the stagnation point shift at higher angles of attack. The high-temperature gas chemistry effects observed in flight, which include lower effective specific heat ratios, probably combined to eliminate the phenomena observed in the wind tunnel tests.

In addition, the preflight algorithm, which is based on the wind tunnel data to Mach 10, calculates the model angles of attack and sideslip from the pressures of the current test within 1° and 0.5° , respectively, for angles of attack of about 8° to 45° . With the current data, the base for the flight

algorithm is extended to a significantly higher Mach number.

NASA Langley Research Center
Hampton, VA 23681-0001
August 2, 1993

References

1. Pruett, C. David; Wolf, Henry; Siemers, Paul M., III; and Heck, Michael L.: An Innovative Air Data System for the Space Shuttle Orbiter: Data Analysis Techniques. AIAA-81-2455, Nov. 1981.
2. Wolf, H.; Henry, M. W.; and Siemers, Paul M., III: Shuttle Entry Air Data System (SEADS): Optimization of Preflight Algorithms Based on Flight Results. AIAA-88-2053, May 1988.
3. Siemers, Paul M., III; and Larson, Terry J.: The Space Shuttle Orbiter and Aerodynamic Testing. AIAA Paper 78-790, Apr. 1978.
4. Bradley, P. F.; Siemers, P. M., III; Flanagan, P. F.; and Henry, M. W.: *Pressure Distributions Obtained on a 0.04-Scale and 0.02-Scale Model of the Space Shuttle Orbiter's Forward Fuselage in the Langley 20-Inch Mach 6 Air Tunnel*. NASA TM-84629, 1983.
5. Bradley, P. F.; Siemers, P. M., III; Flanagan, P. F.; and Henry, M. W.: *Pressure Distributions Obtained on a 0.04-Scale and 0.02-Scale Model of the Space Shuttle Orbiter's Forward Fuselage in the Langley Continuous Flow Hypersonic Tunnel*. NASA TM-84630, 1983.
6. Bradley, P. F.; Siemers, P. M., III; Flanagan, P. F.; and Henry, M. W.: *Pressure Distributions Obtained on a 0.04-Scale Model of the Space Shuttle Orbiter's Forward Fuselage in the Langley Unitary Plan Wind Tunnel*. NASA TM-84628, 1983.
7. Siemers, P. M., III; and Henry, M. W.: *Pressure Distributions Obtained on a 0.10-Scale Model of the Space Shuttle Orbiter's Forebody in the AEDC 16T Propulsion Wind Tunnel*. NASA TM-87653, 1986.
8. Siemers, P. M., III; and Henry, M. W.: *Pressure Distributions Obtained on a 0.10-Scale Model of the Space Shuttle Orbiter's Forebody in the Ames Unitary Plan Wind Tunnel*. NASA TM-87654, 1986.
9. Henry, M. W.; Wolf, H.; and Siemers, Paul M., III: An Evaluation of Shuttle Entry Air Data System (SEADS) Flight Pressures: Comparisons With Wind Tunnel and Theoretical Predictions. AIAA-88-2052, May 1988.
10. Arrington, James P.; Joiner, Roy C., Jr.; and Henderson, Arthur, Jr.: *Longitudinal Characteristics of Several Configurations at Hypersonic Mach Numbers in Conical and Contoured Nozzles*. NASA TN D-2489, 1964.
11. Weinstein, Leonard M.; Wagner, Richard D., Jr.; Henderson, Arthur, Jr.; and Ocheltree Stewart L.: Electron Beam Flow Visualization in Hypersonic Helium Flow. *ICIASF '69 Record*, IEEE Publ. 69-C-19 AES, pp. 72–78.

12. Erickson, Wayne D.: *Real-Gas Correction Factors for Hypersonic Flow Parameters in Helium*. NASA TN D-462, 1960.
13. Shinn, Judy L.: *Comparison of Predicted and Experimental Real-Gas Pressure Distributions on Space Shuttle Orbiter Nose for Shuttle Entry Air Data System*. NASA TP-1627, 1980.
14. Goldberg, Theodore J.; Ashby, George C., Jr.; and Hondros, James G.: *Center-Line Pressure Distributions on Two-Dimensional Bodies With Leading-Edge Angles Greater Than That for Shock Detachment at Mach Number 6 and Angles of Attack up to 25°*. NASA TN D-1793, 1963.
15. Ashby, George C., Jr.; and Goldberg, Theodore J.: *Application of Generalized Newtonian Theory to Three-Dimensional Sharp-Nose Shock-Detached Bodies at Mach 6 for Angles of Attack up to 25°*. NASA TN D-2550, 1962.

Table I. Orifice Locations

Orifice	x , in.	y , in.	z , in.	η_i , deg	λ_i , deg	ϕ_i , deg
1	0.043	0	0.185	-22.73	-1.13	-92.99
2	.011	0	.094	-14.06	-1.20	-94.96
3	0	0	0	-1.58	-.38	-103.98
4	.01	0	-.093	13.91	-.38	91.57
5	.04	0	-.184	27.00	-.99	92.17
6	.088	0	-.267	37.22	-1.31	92.17
7	.149	0	-.342	44.89	-1.52	92.16
8	.22	0	-.408	49.42	-1.69	92.23
9	.089	-.270	-.082	34.54	-33.49	166.71
10	.046	-.185	-.088	25.17	-22.36	153.45
11	.018	-.095	-.092	18.47	-13.59	137.85
12	.018	.095	-.092	17.35	11.05	50.01
13	.046	.185	-.088	24.67	22.70	22.39
14	.089	.270	-.082	32.25	31.47	11.99
15	.645	-.063	.748	57.22	-2.94	-93.49
16	.644	-.731	-.225	59.28	-57.55	169.00
17	.644	.731	-.225	59.10	57.53	10.50
18	.64	-.105	-.648	66.93	-5.01	95.45
19	2.804	-1.499	-.170	76.15	-76.15	-179.74
20	2.804	1.499	-.170	76.13	76.11	.73
25	2.066	0	1.422	67.28	-.99	-91.08
27	.2	0	.410	43.81	-.30	-90.43
30	2.14	0	-1.050	83.00	.16	89.84
31	.306	-.504	-.050	50.02	-50.02	179.31
34	.306	.504	-.050	49.75	49.75	.35
35	2.511	-1.362	-.578	74.35	-62.15	156.66
36	2.523	-1.226	-.767	77.14	-41.88	133.21
37	2.628	-.817	-.990	83.22	-14.97	105.09
38	2.603	-.519	-1.041	83.85	-7.63	97.68
39	2.624	-.099	-1.071	84.48	-1.48	91.48
44	3.124	.018	1.861	67.82	-.08	-90.09
45	2.514	.020	1.610	65.08	.59	-89.35
46	1.735	-1.185	.090	72.07	-72.04	-179.08
47	2.631	-1.451	-.356	74.52	-73.71	174.87
48	3.747	-1.718	.656	77.61	-77.58	-179.22
49	3.747	1.718	.656	77.96	77.96	.26

Table II. Model Attitudes and Tunnel Flow Parameters

[Pressures are in psia]

Run	α , deg	β , deg	$p_{t,\infty}$	$T_{t,\infty}$, °F	$P_{t,2}$	M_∞	p_∞	q_∞
78	0	0	2002.62	60.79	5.047	21.16	0.007976	2.8617
80	5.0	↓	2003.62	66.00	5.302	20.81	.008662	3.0074
74	10.0		2002.37	56.99	5.349	20.76	.008784	3.0316
76	15.0		2005.62	71.48	5.190	20.96	.008341	2.9402
70	20.0		2001.12	61.49	5.020	21.19	.007912	2.8476
68	25.0		2000.62	57.46	5.007	21.22	.007872	2.8389
67	30.0		1999.62	54.51	4.9405	21.31	.007703	2.8015
65	35.0		2003.12	58.04	4.9628	21.29	.007752	2.8144
56	39.5		2000.12	57.34	4.9355	21.32	.007687	2.7982
47	40.0		2000.62	70.95	4.9301	21.31	.007670	2.7949
51	40.7		2000.12	73.42	4.9288	21.31	.007669	2.7942
54	45.0		1984.64	49.92	4.8404	21.41	.007484	2.7448
60	50.0		2000.87	64.15	4.9429	21.30	.007707	2.8032
89	5.0	-5.0	2003.87	59.20	5.0289	21.19	.007923	2.8515
87	↓	-3.0	2002.37	53.89	5.1157	21.08	.008150	2.8994
86		-1.5	2003.12	51.77	5.4419	20.64	.009048	3.0868
82		0	2002.12	61.76	5.3441	20.75	.008783	3.0312
91		1.5	2002.62	65.83	5.3660	20.72	.008828	3.0400
94		3.0	2003.62	53.10	5.2333	20.92	.008475	2.9674
97		5.0	2007.87	56.81	5.1246	21.08	.008190	2.9114
116	20.0	-5.0	1998.38	37.01	4.8885	21.41	.007570	2.7718
114	↓	-3.0	2007.62	50.18	4.9251	21.37	.007641	2.7926
113		-1.5	2007.62	48.77	4.9468	21.34	.007697	2.8046
111		0	2003.87	45.23	4.9481	21.33	.007719	2.8074
117		1.5	1999.12	37.81	4.9479	21.32	.007719	2.8048
119		3.0	1995.13	45.32	4.9471	21.30	.007739	2.8071
121		5.0	1999.37	47.35	4.9617	21.29	.007756	2.8131
104	35.0	-5.0	2003.12	49.65	4.8541	21.46	.007464	2.7503
102	↓	-3.0	2004.12	51.95	4.8533	21.46	.007467	2.7517
101		-1.5	2004.87	52.13	4.8649	21.44	.007488	2.7567
99		0	2004.87	59.02	4.8827	21.41	.007542	2.7687
106		1.5	2004.37	51.33	4.8889	21.41	.007559	2.7720
107		3.0	2002.87	47.71	4.8920	21.40	.007569	2.7740
109		5.0	2004.62	40.72	4.9088	21.39	.007612	2.7844
128	40.0	-5.0	2003.12	37.45	4.8033	21.55	.007341	2.7242
126	↓	-3.0	2000.87	35.95	4.8210	21.52	.007385	2.7332
124		-1.5	1999.62	57.52	4.8216	21.48	.007399	2.7355
123		0	1999.87	49.03	4.8402	21.47	.007434	2.7418
129		1.5	2002.62	34.98	4.8404	21.50	.007436	2.7436

Table III. Pressure Data at $\beta = 0^\circ$

Orifice	Run	M_∞	α , deg	C_{pi}
1	78	21.16	0	1.5070
2				1.6711
3				1.7610
4				1.6465
5				1.3571
6				1.0953
7				.9020
8				.7552
9				1.1500
10				1.3967
11				1.5364
12				1.6002
13				1.4604
14				1.2722
15				.5311
16				.4603
17				.4585
18				.3140
19				.1210
20				.1204
25				.2881
27				
30				.0695
31				.7533
34				.7631
35				.1148
36				.0915
37				.0597
38				.0553
39				.0513
44				.2757
45				.2819
46				.1872
47				.1219
48				.0991
49	↓	↓	↓	.0987

Table III. Continued

Orifice	Run	M_∞	α , deg	C_{pi}
1	80	20.81	5	1.3865
2				1.6033
3				1.7487
4				1.7107
5				1.5332
6				1.2785
7				1.0659
8				.9043
9				1.1439
10				1.4294
11				1.6063
12				1.6934
13				1.5634
14				1.3466
15				.3689
16				.4707
17				.4705
18				.4073
19				.1205
20				.1186
25				.1665
27				
30				.1143
31				.7362
34				.7397
35				.1346
36				.1268
37				.0981
38				.0922
39				.0879
44				.1629
45				.1642
46				.1762
47				.1281
48				.0884
49	↓	↓	↓	.0892

Table III. Continued

Orifice	Run	M_∞	α , deg	C_{pi}
1	74	20.76	10	1.2121
2				1.4610
3				1.6935
4				1.7542
5				1.6179
6				1.4356
7				1.2564
8				1.0760
9				1.1390
10				1.4343
11				1.6398
12				1.6766
13				1.5081
14				1.3018
15				.2644
16				.4860
17				.4944
18				.5325
19				.1241
20				.1229
25				.1041
27				
30				.1727
31				.7207
34				.7249
35				.1578
36				.1698
37				.1528
38				.1462
39				.1411
44				.0985
45				.0998
46				.1701
47				.1370
48				.0811
49	↓	↓	↓	

Table III. Continued

Orifice	Run	M_∞	α , deg	C_{pi}
1	76	20.96	15	1.0797
2				1.3451
3				1.6381
4				1.7537
5				1.7017
6				1.6275
7				1.4294
8				1.2872
9				1.2104
10				1.4850
11				1.6495
12				1.7088
13				1.5262
14				1.2929
15				.1760
16				.5121
17				.5184
18				.7290
19				.1295
20				.1306
25				.0625
27				
30				.2608
31				.7234
34				.7424
35				.1828
36				.2318
37				.2385
38				.2289
39				.2177
44				.0543
45				.0574
46				.1691
47				.1424
48				.0756
49	↓	↓	↓	.0762

Table III. Continued

Orifice	Run	M_∞	α , deg	C_{pi}
1	70	21.19	20	0.9214
2				1.1673
3				1.4904
4				1.7127
5				1.7582
6				1.7004
7				1.5985
8				1.4833
9				1.1714
10				1.4413
11				1.6103
12				1.6605
13				1.4540
14				1.2266
15				.1256
16				.5234
17				.5256
18				.9221
19				.1429
20				.1460
25				.0459
27				
30				
31				.6981
34				.6978
35				.2206
36				.3207
37				
38				
39				
44				.0382
45				.0422
46				.1736
47				.1546
48				.0844
49	↓	↓	↓	.0874

Table III. Continued

Orifice	Run	M_∞	α , deg	C_{pi}
1	68	21.22	25	0.7718
2				1.0205
3				1.3743
4				1.6499
5				1.7595
6				1.7464
7				1.6716
8				1.5780
9				1.1190
10				1.3818
11				1.5504
12				1.5983
13				1.3904
14				1.1694
15				.0857
16				.5090
17				.5184
18				1.0858
19				.1387
20				.1456
25				.0339
27				.2539
30				
31				.6559
34				.6612
35				.2407
36				
37				
38				
39				
44				.0283
45				.0318
46				.1701
47				.1464
48				.0855
49	↓	↓	↓	.0902

Table III. Continued

Orifice	Run	M_∞	α , deg	C_{pi}
1	67	21.31	30	0.6207
2				.8409
3				1.2087
4				1.5434
5				1.7239
6				1.7569
7				1.7272
8				1.6743
9				1.0363
10				1.2836
11				1.4469
12				1.4988
13				1.2964
14				1.0874
15				.0564
16				.4775
17				.5056
18				1.2711
19				.1334
20				.1371
25				.0260
27				.1963
30				
31				.5996
34				.6128
35				.2761
36				
37				
38				
39				
44				.0237
45				.0252
46				.1723
47				.1487
48				.0933
49	↓	↓	↓	.0984

Table III. Continued

Orifice	Run	M_∞	α , deg	C_{pi}
1	65	21.29	35	0.4751
2				.6634
3				1.0160
4				1.3764
5				1.6455
6				1.7450
7				1.7548
8				1.7141
9				.9231
10				1.1458
11				1.2933
12				1.3385
13				1.1487
14				.9589
15				.0447
16				.4567
17				.4812
18				1.3813
19				.1229
20				.1326
25				.0238
27				1407
30				
31				.5308
34				.5448
35				.3011
36				
37				
38				
39				
44				.0244
45				.0245
46				.1713
47				.1489
48				.0970
49	↓	↓	↓	.1043

Table III. Continued

Orifice	Run	M_∞	α , deg	C_{pi}
1	56	21.32	39.5	0.3830
2				.5474
3				.8917
4				1.2778
5				1.5719
6				1.7085
7				1.7597
8				1.7555
9				.8532
10				1.0636
11				1.2022
12				1.2415
13				1.0564
14				.8782
15				.0306
16				.4329
17				.4571
18				1.5100
19				.1207
20				.1212
25				.0189
27				.1005
30				
31				.4881
34				.4927
35				.3205
36				
37				
38				
39				
44				.0183
45				.0199
46				.1598
47				.1515
48				.0951
49	↓	↓	↓	.0981

Table III. Continued

Orifice	Run	M_∞	α , deg	C_{pi}
1	47	21.31	40	0.3772
2				.5389
3				.8773
4				1.2629
5				1.5647
6				1.7064
7				1.7591
8				1.7571
9				.8611
10				1.0513
11				1.1881
12				1.2268
13				1.0436
14				.8685
15				.0326
16				.4314
17				.4563
18				1.5124
19				.1227
20				.1244
25				.0202
27				.0776
30				
31				.4818
34				.4876
35				.3227
36				
37				
38				
39				
44				.0198
45				.0213
46				.1629
47				.1544
48				.0981
49	↓	↓	↓	.1024

Table III. Continued

Orifice	Run	M_∞	α , deg	C_{pi}
1	51	21.31	40.7	0.3639
2				.5242
3				.8551
4				1.2300
5				1.5445
6				1.7031
7				1.7593
8				1.7563
9				.8201
10				1.0236
11				1.1566
12				1.1956
13				1.0175
14				.8465
15				.0308
16				.4273
17				.4502
18				1.5149
19				.1189
20				.1221
25				.0198
27				.0949
30				
31				.4709
34				.4760
35				.3241
36				
37				
38				
39				
44				.0195
45				.0208
46				.1605
47				.1511
48				.0951
49	↓	↓	↓	.0993

Table III. Continued

Orifice	Run	M_∞	α , deg	C_{pi}
1	54	21.41	45	0.2884
2				.4278
3				.7229
4				1.0957
5				1.4115
6				1.6051
7				1.7146
8				1.7500
9				.7367
10				.9103
11				1.0303
12				1.0643
13				.8995
14				.7474
15				.0262
16				.3916
17				.4125
18				1.6428
19				.1168
20				.1216
25				.0190
27				.0696
30				
31				.4110
34				.4195
35				.3323
36				
37				
38				
39				
44				.0190
45				.0196
46				.1472
47				.1469
48				.0949
49	↓	↓	↓	.1023

Table III. Concluded

Orifice	Run	M_∞	α , deg	C_{pi}
1	60	21.30	50	0.1733
2				.3107
3				.5521
4				.9100
5				1.2557
6				1.5023
7				1.6533
8				1.7176
9				.5976
10				.7561
11				.8569
12				.8849
13				.7380
14				.6145
15				.0228
16				.3606
17				.3817
18				1.6552
19				.1185
20				.1192
25				.0180
27				.0461
30				
31				.3411
34				.3505
35				
36				
37				
38				
39				
44				.0189
45				.0186
46				.1294
47				.1539
48				.0962
49	↓	↓	↓	.0994

Table IV. Pressure Data at $\alpha = 5^\circ$

Orifice	Run	M_∞	β , deg	C_{pi}
1	89	21.19	-5	1.3897
2				1.5877
3				1.7364
4				1.7132
5				1.5301
6				1.3135
7				1.1251
8				.9587
9				1.4036
10				1.5862
11				1.6735
12				1.5973
13				1.3521
14				1.1032
15				.3803
16				.6597
17				.3654
18				.4417
19				.2158
20				.0743
25				.1757
27				
30				.1187
31				1.0094
34				.5897
35				.2291
36				.1983
37				.1281
38				.1101
39				.0901
44				.1726
45				.1682
46				.2943
47				.2494
48				.1699
49	↓	↓	↓	.0546

Table IV. Continued

Orifice	Run	M_∞	β , deg	C_{pi}
1	87	21.08	-3	1.3938
2	↓	↓	↓	1.5947
3				1.7333
4				1.6992
5				1.5099
6				1.2910
7				1.1060
8				.9461
9				1.3690
10				1.6144
11				1.6931
12				1.5918
13				1.3984
14				1.1836
15				.3720
16				.5882
17				.4021
18				.4314
19				.1750
20				.0910
25				.1732
27				
30				.1169
31				.9003
34				.6419
35				.1892
36				.1670
37				.1143
38				.1019
39				.0875
44				.1592
45				.1678
46				.2355
47				.1828
48				.1309
49				.0666

Table IV. Continued

Orifice	Run	M_∞	β , deg	C_{pi}
1	86	20.64	-1.5	1.3837
2				1.5984
3				1.7432
4				1.6952
5				1.4658
6				1.2253
7				1.0357
8				.8835
9				1.2373
10				1.4851
11				1.6190
12				1.5661
13				1.3514
14				1.1421
15				.3503
16				.5247
17				.4080
18				.4044
19				.1437
20				.0987
25				.1629
27				
30				.1110
31				.7866
34				.6540
35				.1566
36				.1409
37				.1020
38				
39				.0837
44				.1550
45				.1589
46				.1976
47				.1498
48				.1070
49	↓	↓	↓	.0726

Table IV. Continued

Orifice	Run	M_∞	β , deg	C_{pi}
1	82	20.75	0	1.4014
2				1.5904
3				1.7324
4				1.7354
5				1.5016
6				1.2374
7				1.0401
8				.8895
9				1.1785
10				1.4582
11				1.6239
12				1.6566
13				1.4806
14				1.2565
15				.3574
16				.4886
17				.4560
18				.4065
19				.1240
20				.1185
25				.1655
27				
30				.1137
31				.7465
34				.7175
35				.1379
36				.1282
37				.0977
38				.0915
39				.0861
44				.1670
45				.1628
46				.1758
47				.1323
48				.0913
49	↓	↓	↓	.0896

Table IV. Continued

Orifice	Run	M_∞	β , deg	C_{pi}
1	91	20.72	1.5	1.3669
2				1.5711
3				1.7509
4				1.7051
5				1.4633
6				1.2228
7				1.0367
8				.8881
9				1.1109
10				1.3789
11				1.5555
12				1.6813
13				1.5366
14				1.3279
15				.3525
16				.4420
17				.5015
18				.4039
19				.1061
20				.1357
25				.1637
27				
30				.1117
31				.7109
34				.7661
35				.1198
36				.1018
37				.0922
38				.0862
39				.0824
44				.1573
45				.1607
46				.1550
47				.1128
48				.0759
49	↓	↓	↓	.1039

Table IV. Continued

Orifice	Run	M_∞	β , deg	C_{pi}
1	94	20.92	3	1.3801
2				1.5863
3				1.7518
4				1.7028
5				1.4809
6				1.2537
7				1.0696
8				.9178
9				1.1150
10				1.3810
11				1.5465
12				1.7153
13				1.6142
14				1.4199
15				.3586
16				.4293
17				.5534
18				.4131
19				.0955
20				.1596
25				.1684
27				
30				.1158
31				.6802
34				.8527
35				.1100
36				.1081
37				.0901
38				.0871
39				.0844
44				.1555
45				.1661
46				.1418
47				.1024
48				.0680
49	↓	↓	↓	.1229

Table IV. Concluded

Orifice	Run	M_∞	β , deg	C_{pi}
1	97	21.08	5	1.4004
2				1.6003
3				1.7418
4				1.7116
5				1.5140
6				1.2926
7				1.1036
8				.9429
9				1.1002
10				1.3947
11				1.5665
12				1.7120
13				1.6217
14				1.4742
15				.3615
16				.3830
17				.6166
18				.4149
19				.0812
20				.1924
25				.1724
27				
30				.1176
31				.6212
34				.9591
35				.0953
36				.0970
37				.0872
38				.0867
39				.0849
44				.1608
45				.1699
46				.1212
47				.0868
48				.0578
49	↓	↓	↓	.1505

Table V. Pressure Data at $\alpha = 20^\circ$

Orifice	Run	M_∞	β , deg	C_{pi}
1	116	21.41	-5	0.9305
2				1.1836
3				1.5060
4				1.7195
5				1.7573
6				1.6857
7				1.5662
8				1.4295
9				1.3450
10				1.5751
11				1.6905
12				1.5982
13				1.3384
14				1.0852
15				.1337
16				.7047
17				.3948
18				.9432
19				.2421
20				.0841
25				.0456
27				
30				
31				.8828
34				.5529
35				
36				
37				
38				
39				
44				.0407
45				.0417
46				.2775
47				.2699
48				.1539
49	↓	↓	↓	.0478

Table V. Continued

Orifice	Run	M_∞	β , deg	C_{pi}
1	114	21.37	-3	0.9407
2				1.1875
3				1.5080
4				1.7220
5				1.7564
6				1.6870
7				1.5733
8				1.4446
9				1.2807
10				1.5262
11				1.6629
12				1.6296
13				1.3907
14				1.1472
15				.1308
16				.6345
17				.4529
18				.9539
19				.2019
20				.1074
25				.0464
27				
30				
31				.8130
34				.6192
35				.2925
36				
37				
38				
39				
44				.0405
45				.0426
46				.2338
47				.2219
48				.1233
49	↓	↓	↓	.0615

Table V. Continued

Orifice	Run	M_∞	β , deg	C_{pi}
1	113	21.34	-1.5	0.9406
2				1.1853
3				1.5069
4				1.7223
5				1.7564
6				1.6871
7				1.5723
8				1.4457
9				1.2399
10				1.4959
11				1.6462
12				1.6464
13				1.4228
14				1.1865
15				.1290
16				.5913
17				.4850
18				.9484
19				.1777
20				.1221
25				.0464
27				
30				
31				.7691
34				.6555
35				.2629
36				
37				
38				
39				
44				.0397
45				.0426
46				.2104
47				.1955
48				.1062
49	↓	↓	↓	.0716

Table V. Continued

Orifice	Run	M_∞	β , deg	C_{pi}
1	111	21.33	0	0.9400
2				1.1841
3				1.5064
4				1.7226
5				1.7563
6				1.6874
7				1.5724
8				1.4457
9				1.1971
10				1.4637
11				1.6264
12				1.6653
13				1.4579
14				1.2306
15				.1209
16				.5442
17				.5231
18				.9404
19				.1474
20				.1382
25				.0580
27				
30				
31				.7221
34				.6990
35				.2316
36				.3302
37				
38				
39				
44				.0373
45				.0407
46				.1830
47				.1631
48				.0830
49	↓	↓	↓	.0828

Table V. Continued

Orifice	Run	M_∞	β , deg	C_{pi}
1	117	21.32	1.5	0.9382
2				1.1829
3				1.5060
4				1.7226
5				1.7562
6				1.6855
7				1.5678
8				1.4398
9				1.1516
10				1.4292
11				1.6056
12				1.6840
13				1.4940
14				1.2752
15				.1260
16				.4970
17				.5659
18				.9300
19				.1284
20				.1645
25				.0462
27				
30				
31				.6749
34				.7452
35				.2022
36				.3018
37				
38				
39				
44				.0392
45				.0425
46				.1618
47				.1382
48				.0748
49	↓	↓	↓	.1019

Table V. Continued

Orifice	Run	M_∞	β , deg	C_{pi}
1	119	21.30	3	0.9362
2				1.1815
3				1.5035
4				1.7205
5				1.7546
6				1.6826
7				1.5634
8				1.4338
9				1.1067
10				1.3942
11				1.5838
12				1.7003
13				1.5265
14				1.3163
15				.1251
16				.4670
17				.6094
18				.9188
19				.1108
20				.1920
25				.0460
27				
30				
31				.6297
34				.7885
35				.1747
36				.2716
37				
38				.3407
39				
44				.0400
45				.0423
46				.1419
47				.1173
48				.0632
49	↓	↓	↓	.1198

Table V. Concluded

Orifice	Run	M_∞	β , deg	C_{pi}
1	121	21.29	5	0.9319
2				1.1821
3				1.5023
4				1.7210
5				1.7562
6				1.6817
7				1.5601
8				1.4268
9				1.0474
10				1.3463
11				1.5540
12				1.7274
13				1.5791
14				1.3811
15				.1251
16				.4044
17				.6780
18				.9068
19				.0892
20				.2284
25				.0450
27				
30				
31				.5701
34				.8534
35				.1471
36				.2369
37				.3238
38				.3333
39				
44				.0397
45				.0413
46				.1195
47				.0940
48				.0499
49	↓	↓	↓	.1483

Table VI. Pressure Data at $\alpha = 35^\circ$

Orifice	Run	M_∞	β , deg	C_{pi}
1	104	21.46	-5	0.5062
2				.7113
3				1.0800
4				1.4340
5				1.6725
6				1.7514
7				1.7524
8				1.7034
9				1.0912
10				1.2964
11				1.4105
12				1.3308
13				1.0901
14				.8710
15				.0433
16				.6098
17				.3676
18				1.3796
19				.2231
20				.0742
25				.0214
27				.1470
30				
31				.6879
34				.4460
35				
36				
37				
38				
39				
44				.0199
45				.0207
46				.2587
47				.2469
48				.1666
49	↓	↓	↓	.0576

Table VI. Continued

Orifice	Run	M_∞	β , deg	C_{pi}
1	102	21.46	-3	0.5060
2				.7112
3				1.0822
4				1.4366
5				1.6729
6				1.7509
7				1.7520
8				1.7064
9				1.0420
10				1.2587
11				1.3868
12				1.3574
13				1.1334
14				.9212
15				.0445
16				.5529
17				.4096
18				1.3800
19				.1831
20				.0927
25				.0217
27				.1473
30				
31				.6345
34				.4890
35				
36				
37				
38				
39				
44				.0202
45				.0215
46				.2245
47				.2105
48				.1389
49	↓	↓	↓	.0729

Table VI. Continued

Orifice	Run	M_∞	β , deg	C_{pi}
1	101	21.44	-1.5	0.5035
2				.7092
3				1.0770
4				1.4391
5				1.6751
6				1.7524
7				1.7526
8				1.7064
9				1.0077
10				1.2333
11				1.3738
12				1.3739
13				1.1608
14				.9545
15				.0436
16				.5151
17				.4393
18				1.3794
19				.1598
20				.1077
25				.0217
27				1486
30				
31				.5982
34				.5187
35				
36				
37				
38				
39				
44				.0209
45				.0221
46				.2029
47				.1874
48				.1219
49	↓	↓	↓	.0846

Table VI. Continued

Orifice	Run	M_∞	β , deg	C_{pi}
1	99	21.41	0	0.4987
2				.7036
3				1.0749
4				1.4379
5				1.6733
6				1.7512
7				1.7517
8				1.7067
9				.9685
10				1.2028
11				1.3544
12				1.3880
13				1.1884
14				.9875
15				.0427
16				.4769
17				.4713
18				1.3709
19				.1368
20				.1248
25				.0224
27				.1452
30				
31				.5595
34				.5501
35				.3200
36				
37				
38				
39				
44				.0224
45				.0230
46				.1797
47				.1636
48				.1032
49	↓	↓	↓	.0977

Table VI. Continued

Orifice	Run	M_∞	β , deg	C_{pi}
1	106	21.41	1.5	0.4967
2				.6973
3				1.0720
4				1.4350
5				1.6719
6				1.7519
7				1.7519
8				1.7074
9				.9263
10				1.1661
11				1.3311
12				1.4055
13				1.2208
14				1.0270
15				.0418
16				.4362
17				.5112
18				1.3664
19				.1160
20				.1480
25				.0218
27				.1458
30				
31				.5170
34				.5863
35				.2897
36				
37				
38				
39				
44				.0211
45				.0216
46				.1573
47				.1393
48				.0862
49	↓	↓	↓	.1163

Table VI. Continued

Orifice	Run	M_∞	β , deg	C_{pi}
1	107	21.40	3	0.4940
2				.6915
3				1.0658
4				1.4301
5				1.6682
6				1.7496
7				1.7522
8				1.7066
9				.8847
10				1.1323
11				1.3065
12				1.4210
13				1.2517
14				1.0646
15				.0413
16				.4008
17				.5511
18				1.3551
19				.0968
20				.1720
25				.0210
27				.1456
30				
31				.4797
34				.6226
35				.2624
36				
37				
38				
39				
44				.0193
45				.0199
46				.1360
47				.1190
48				.0722
49	↓	↓	↓	.1348

Table VI. Concluded

Orifice	Run	M_∞	β , deg	C_{pi}
1	109	21.39	5	0.4894
2				.6842
3				1.0525
4				1.4208
5				1.6622
6				1.7468
7				1.7519
8				1.7029
9				.8245
10				1.0830
11				1.2712
12				1.4377
13				1.2896
14				1.1145
15				.0419
16				.3556
17				.6059
18				1.3421
19				.0753
20				.2081
25				.0212
27				.1443
30				
31				.4339
34				.6755
35				.2256
36				
37				
38				
39				
44				.0198
45				.0203
46				.1104
47				.0967
48				.0601
49	↓	↓	↓	.1626

Table VII. Pressure Data at $\alpha = 40^\circ$

Orifice	Run	M_∞	β , deg	C_{pi}
1	128	21.55	-5	0.3996
2				.5756
3				.9152
4				1.2879
5				1.5752
6				1.7111
7				1.7597
8				1.7532
9				.9833
10				1.1700
11				1.2714
12				1.1929
13				.9673
14				.7670
15				.0327
16				.5691
17				.3364
18				1.5438
19				.2091
20				.0736
25				.0214
27				.1003
30				
31				.6139
34				.3926
35				
36				
37				
38				
39				
44				.0218
45				.0231
46				.2472
47				.2425
48				.1669
49	↓	↓	↓	.0567

Table VII. Continued

Orifice	Run	M_∞	β , deg	C_{pi}
1	126	21.52	-3	0.4060
2				.5820
3				.9243
4				1.2955
5				1.5791
6				1.7128
7				1.7603
8				1.7549
9				.9491
10				1.1464
11				1.2582
12				1.2158
13				1.0004
14				.8039
15				.0359
16				.5237
17				.3654
18				1.5298
19				.1816
20				.0896
25				.0248
27				.1049
30				
31				.5752
34				.4221
35				
36				
37				
38				
39				
44				.0257
45				.0275
46				.2196
47				.2152
48				.1456
49	↓	↓	↓	.0701

Table VII. Continued

Orifice	Run	M_∞	β , deg	C_{pi}
1	124	21.48	-1.5	0.3977
2				.5688
3				.9091
4				1.2811
5				1.5650
6				1.7025
7				1.7578
8				1.7542
9				.8985
10				1.1016
11				1.2258
12				1.2210
13				1.0201
14				.8331
15				.0348
16				.4920
17				.4000
18				1.5124
19				.1565
20				.1063
25				.0244
27				.1026
30				
31				.5308
34				.4495
35				
36				
37				
38				
39				
44				.0261
45				.0275
46				.1924
47				.1900
48				.1245
49	↓	↓	↓	.0848

Table VII. Continued

Orifice	Run	M_∞	β , deg	C_{pi}
1	123	21.47	0	0.4122
2				.5852
3				.9250
4				1.2923
5				1.5716
6				1.7084
7				1.7604
8				1.7587
9				.8689
10				1.0815
11				1.2171
12				1.2492
13				1.0598
14				.8773
15				.0371
16				.4528
17				.4392
18				1.5038
19				.1336
20				.1243
25				.0287
27				.1087
30				
31				.4987
34				.4853
35				.3377
36				
37				
38				
39				
44				.0301
45				.0319
46				.1689
47				.1659
48				.1057
49	↓	↓	↓	.1004

Table VII. Concluded

Orifice	Run	M_∞	β , deg	C_{pi}
1	129	21.50	1.5	0.4092
2				.5873
3				.9273
4				1.2936
5				1.5722
6				1.7065
7				1.7591
8				1.7577
9				.8362
10				1.0561
11				1.2000
12				1.2692
13				1.0957
14				.9195
15				.0397
16				.4031
17				.4813
18				1.4988
19				.1132
20				.1466
25				.0294
27				.1103
30				
31				.4668
34				.5235
35				.3075
36				
37				
38				
39				
44				.0305
45				.0318
46				.1466
47				.1439
48				.0884
49	↓	↓	↓	.1197

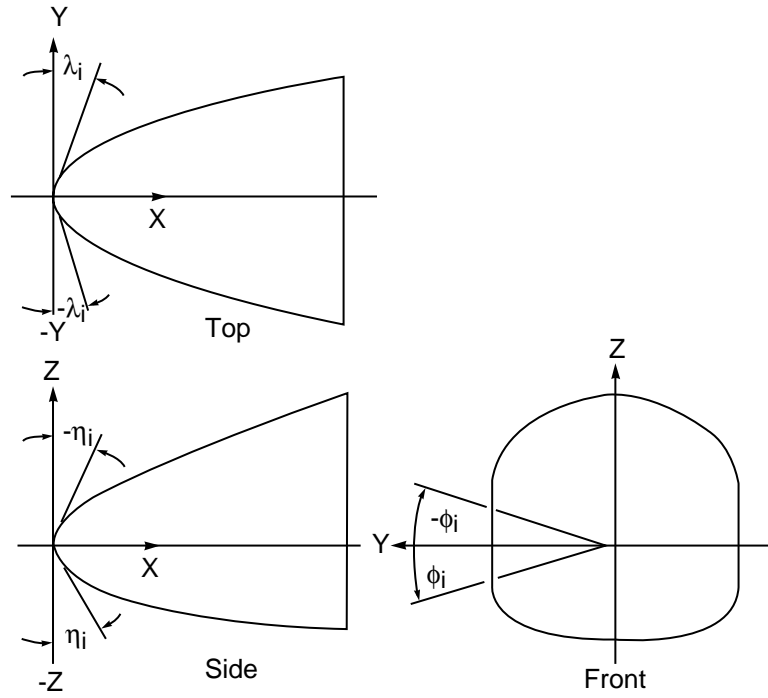


Figure 2. Model coordinate system. Note: negative sign on η_i above centerline is for this paper only.

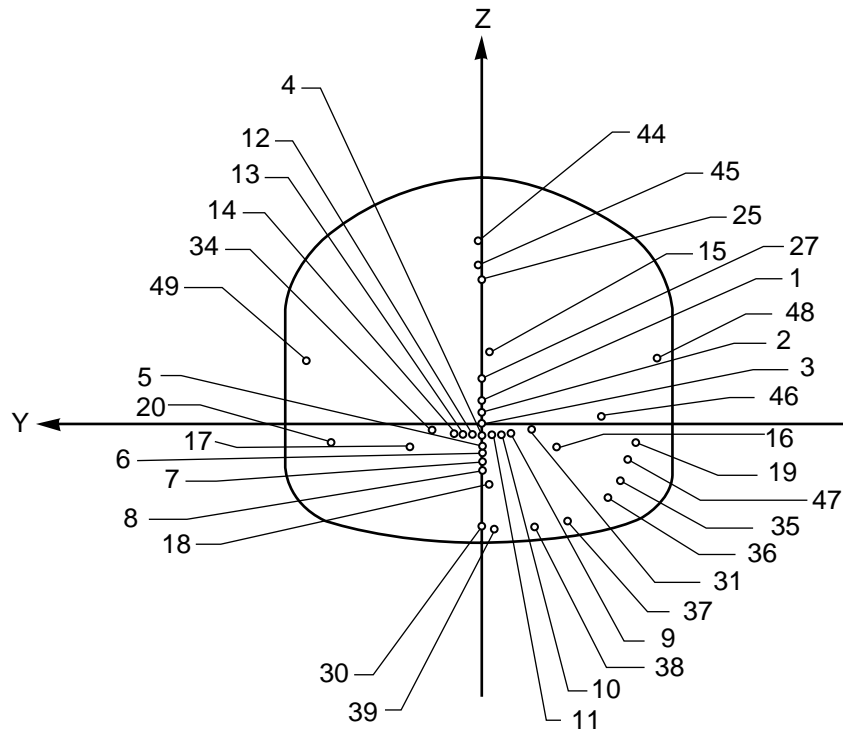
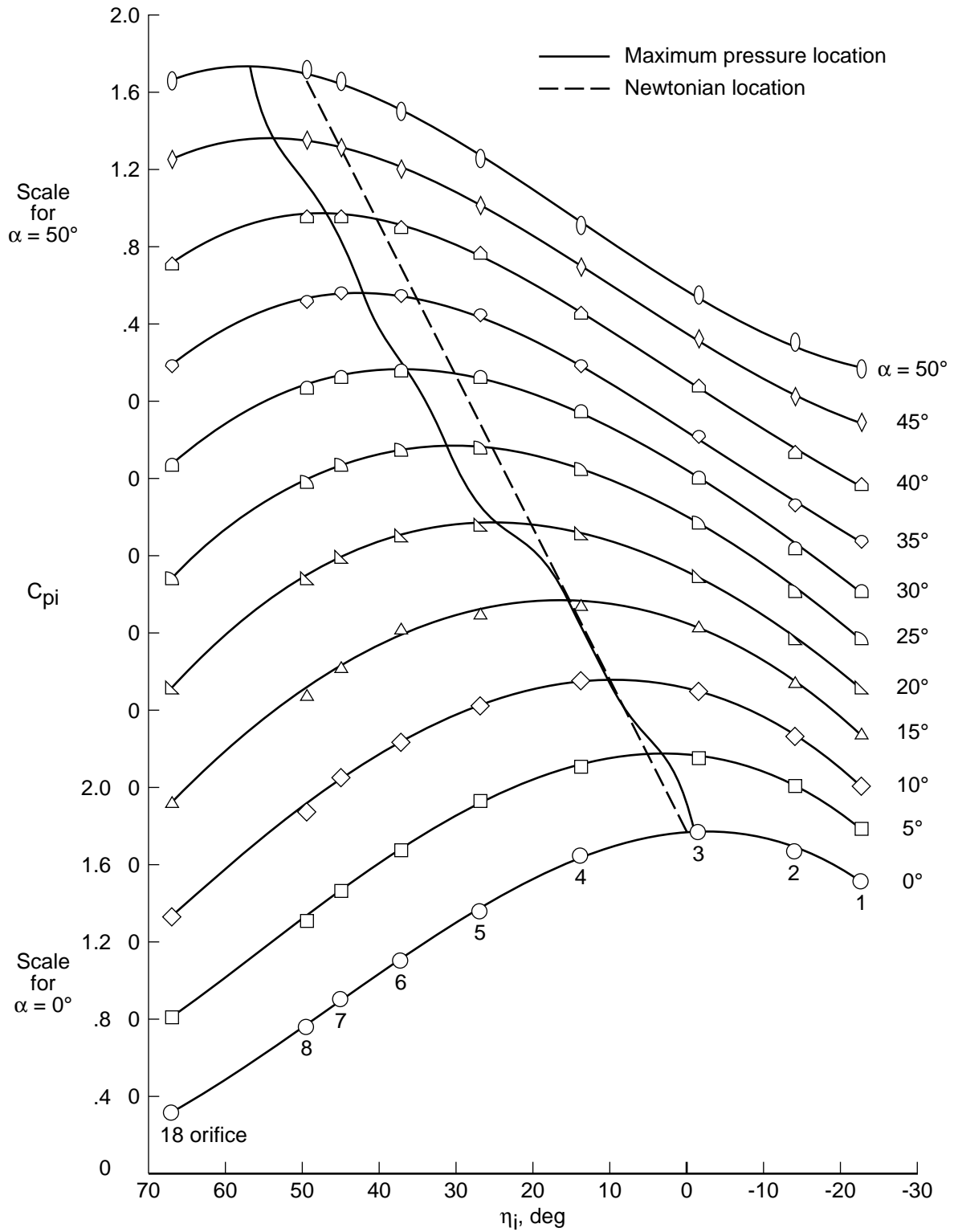
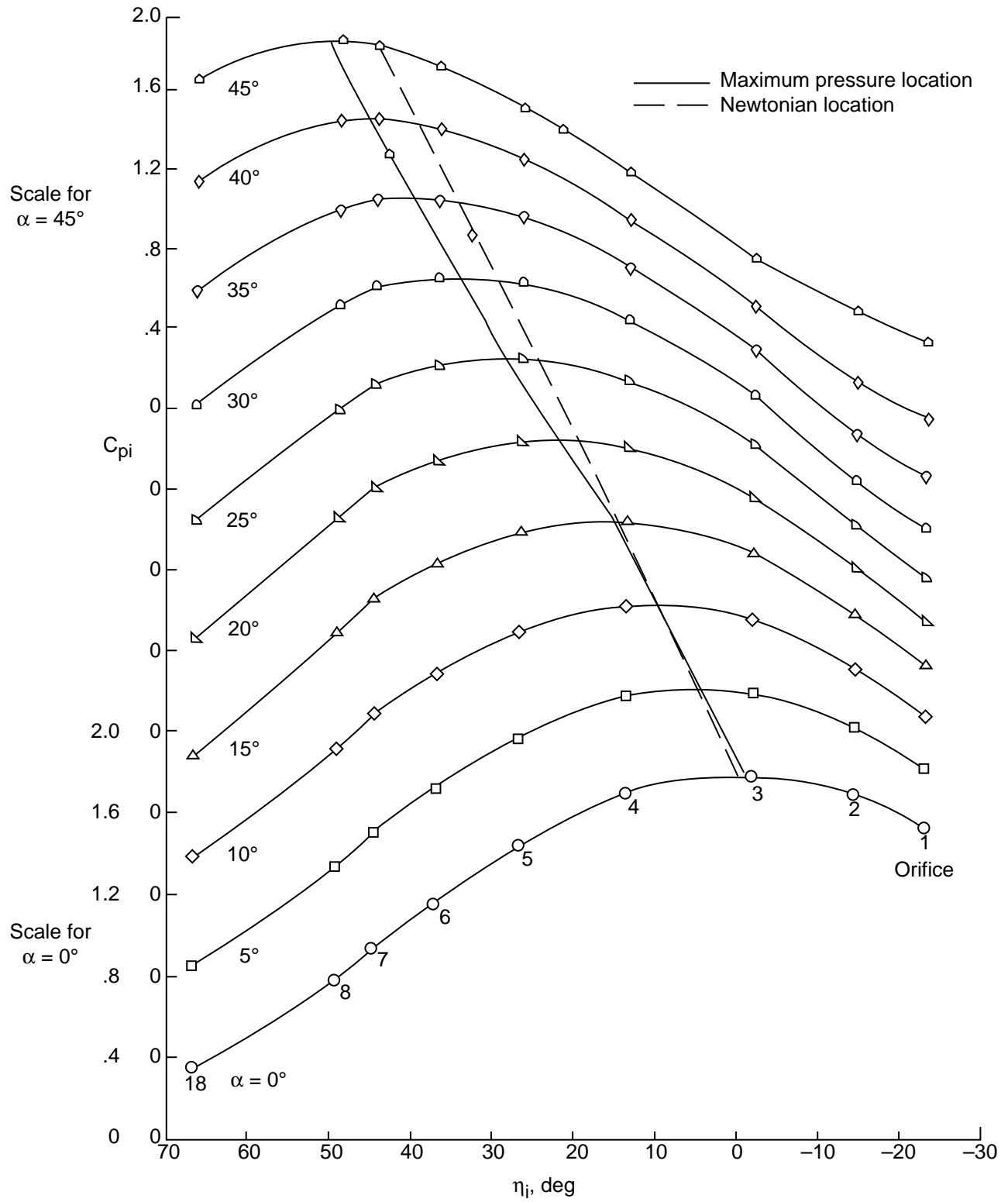


Figure 3. Front of model with orifice locations. See table I.



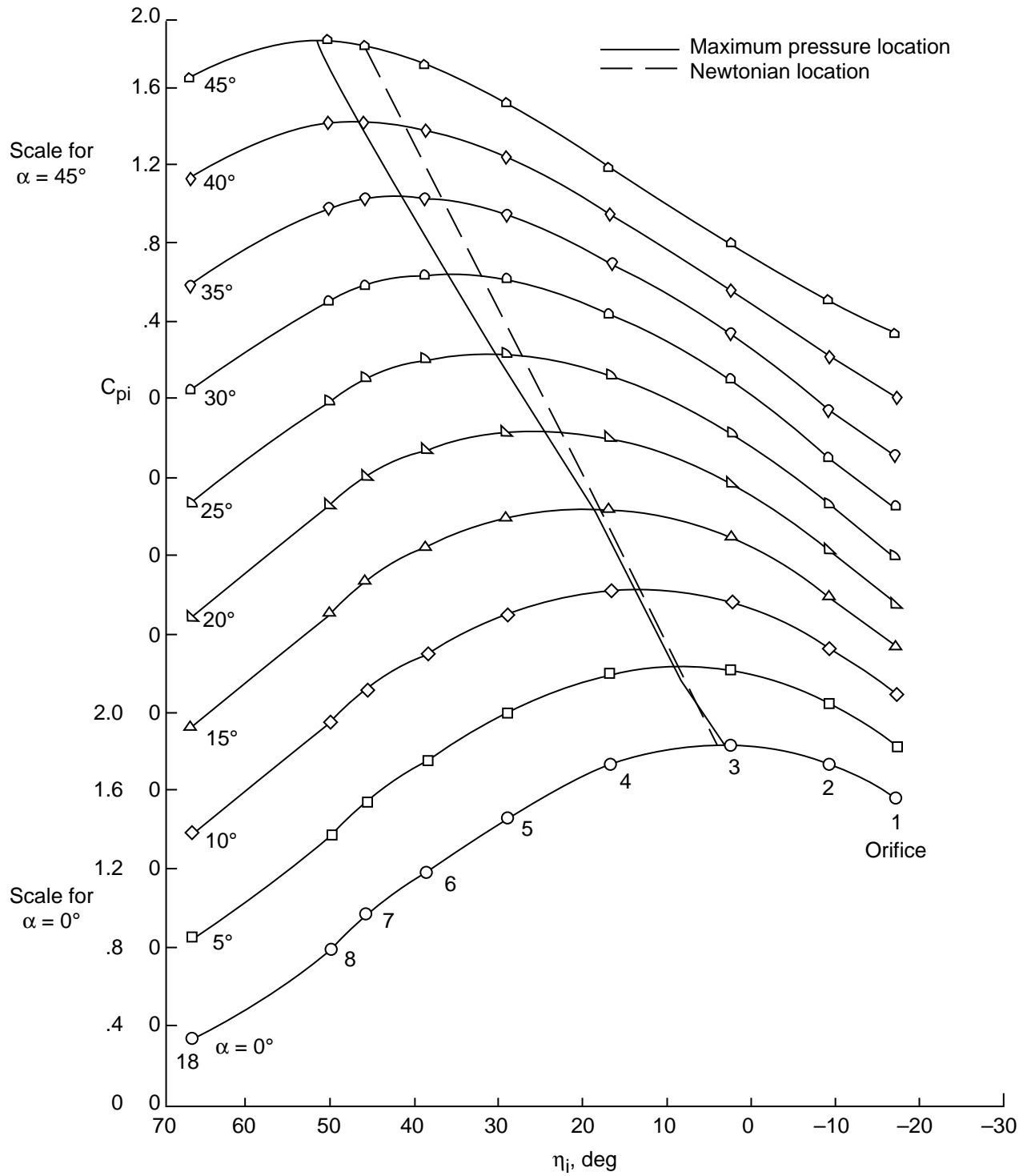
(a) $M_\infty = 21.5$ in helium.

Figure 5. Measured pressure distributions in plane of symmetry at various α 's and M_∞ 's.



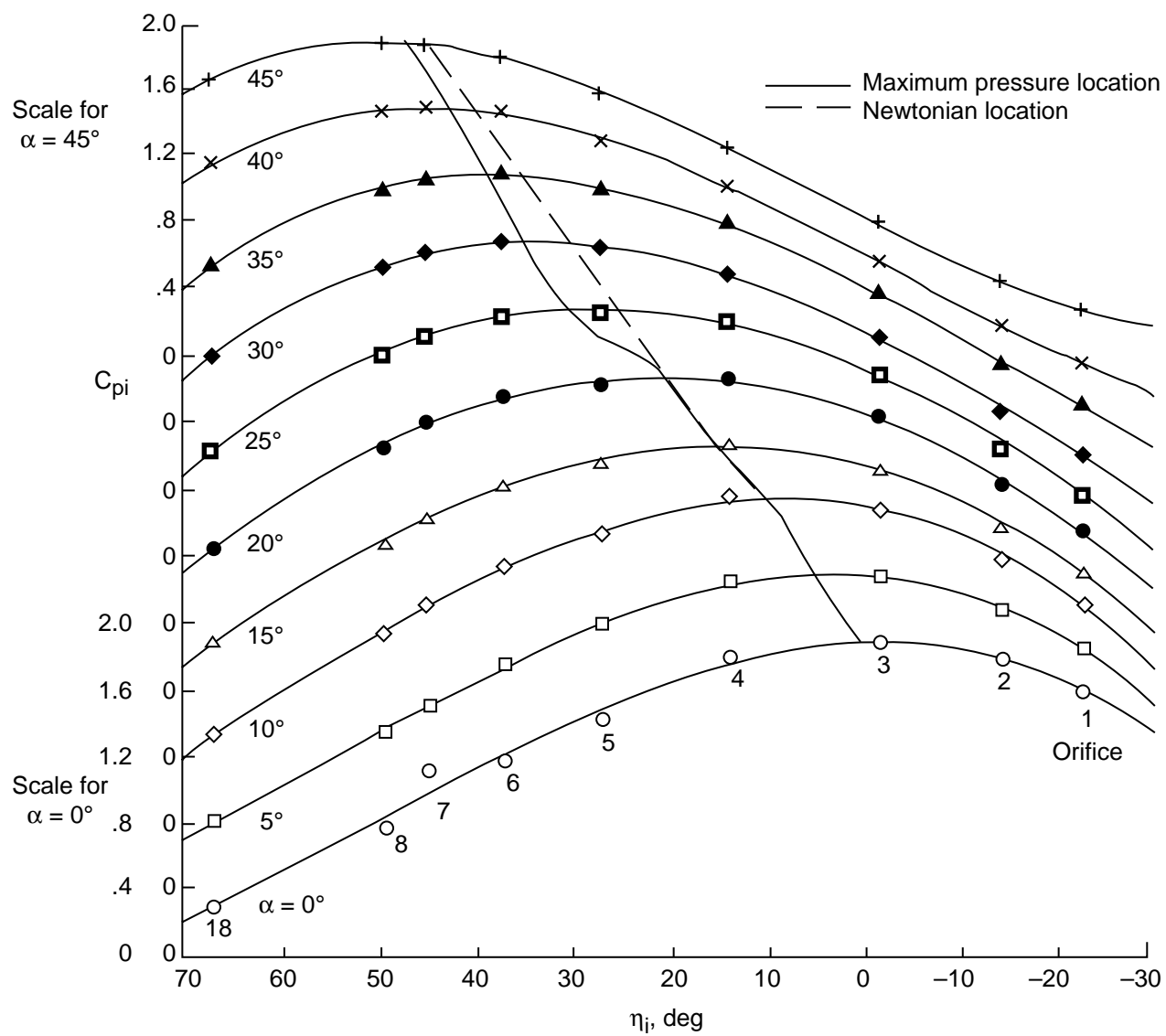
(b) $M_\infty = 10$ in air (ref. 5).

Figure 5. Continued.



(c) $M_\infty = 6$ in air (ref. 4).

Figure 5. Continued.



(d) $M_\infty = 6$ in CF_4 .

Figure 5. Concluded.

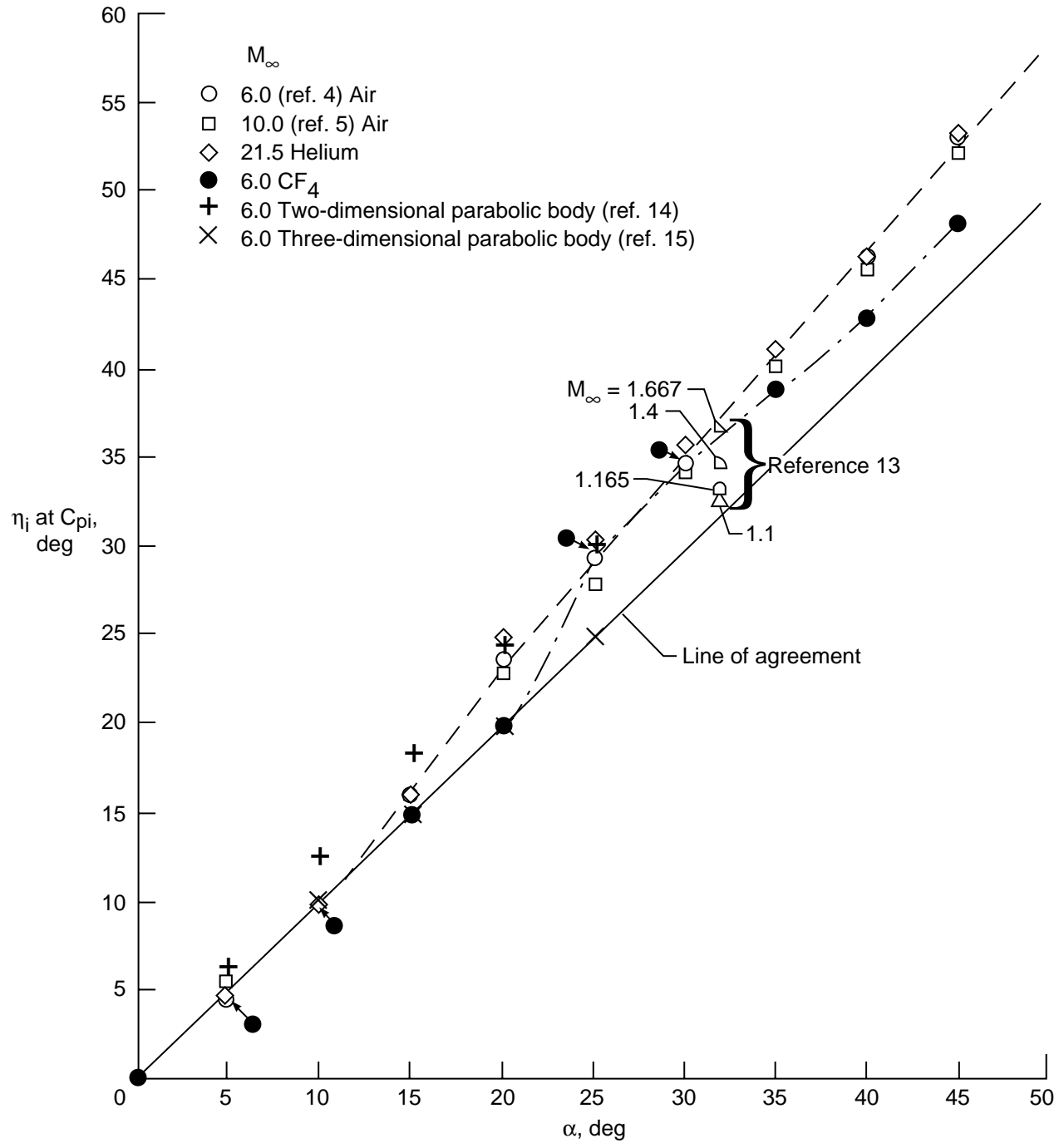


Figure 6. Centerline Newtonian versus faired surface slope angles of maximum pressure for various α 's and M_∞ 's.

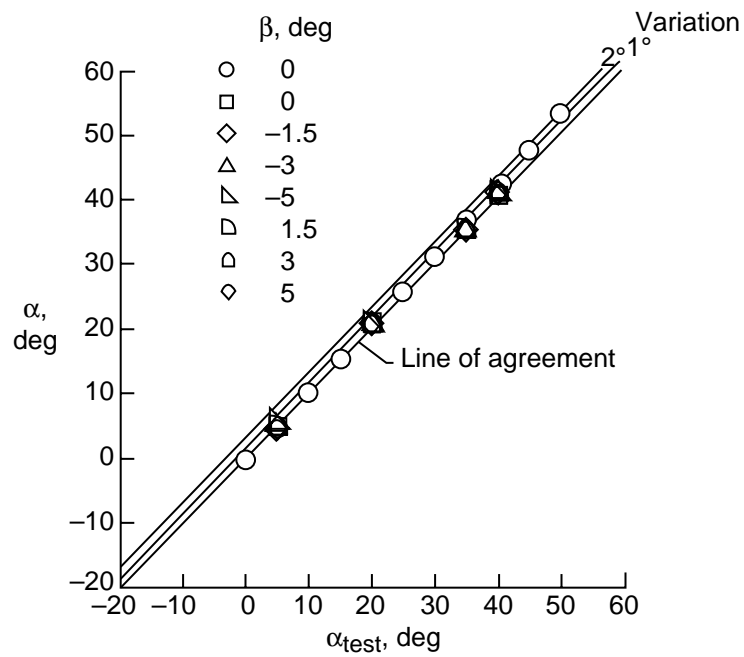
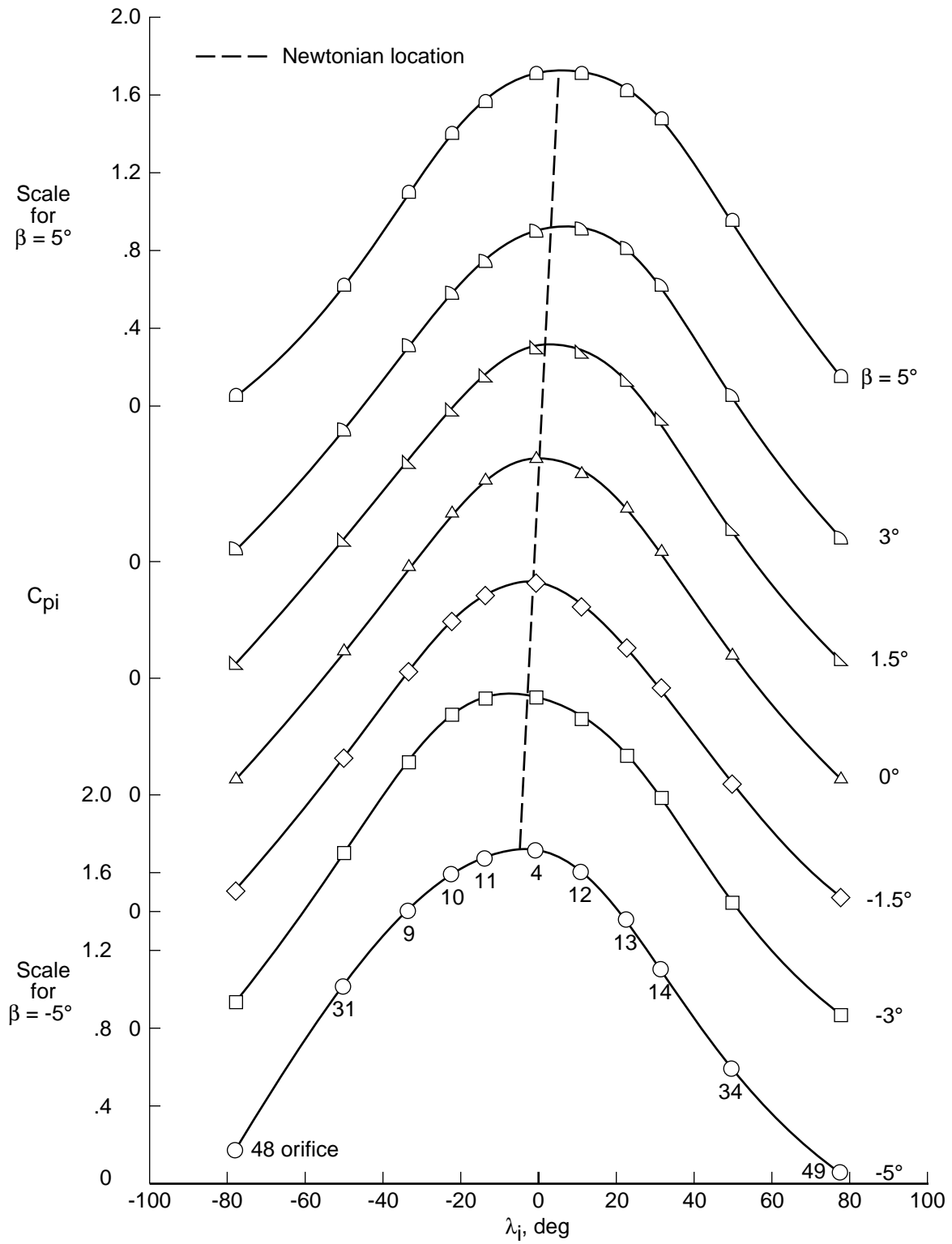
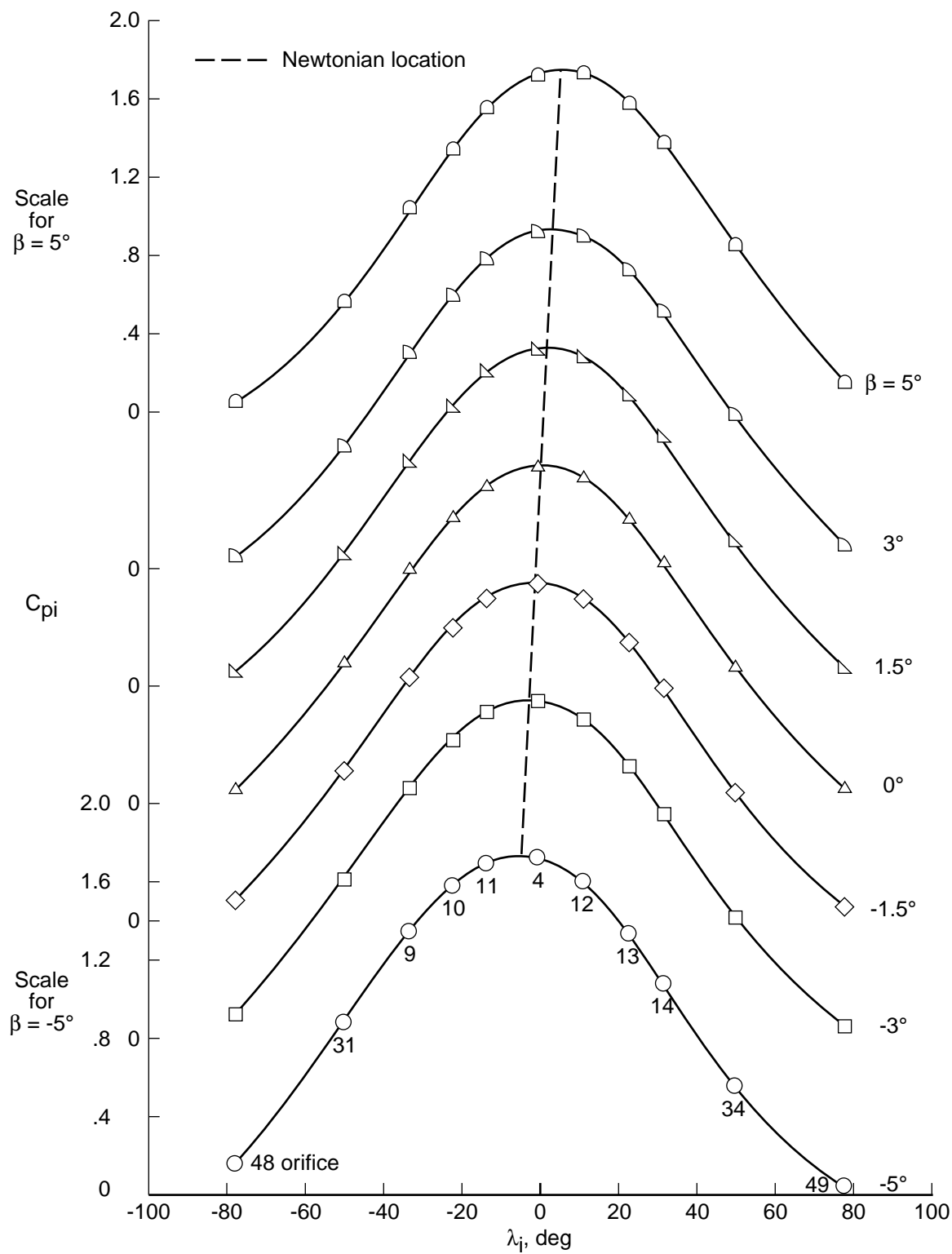


Figure 7. Model α 's set during tests versus predictions by SEAD algorithm and pressure distributions of these tests.

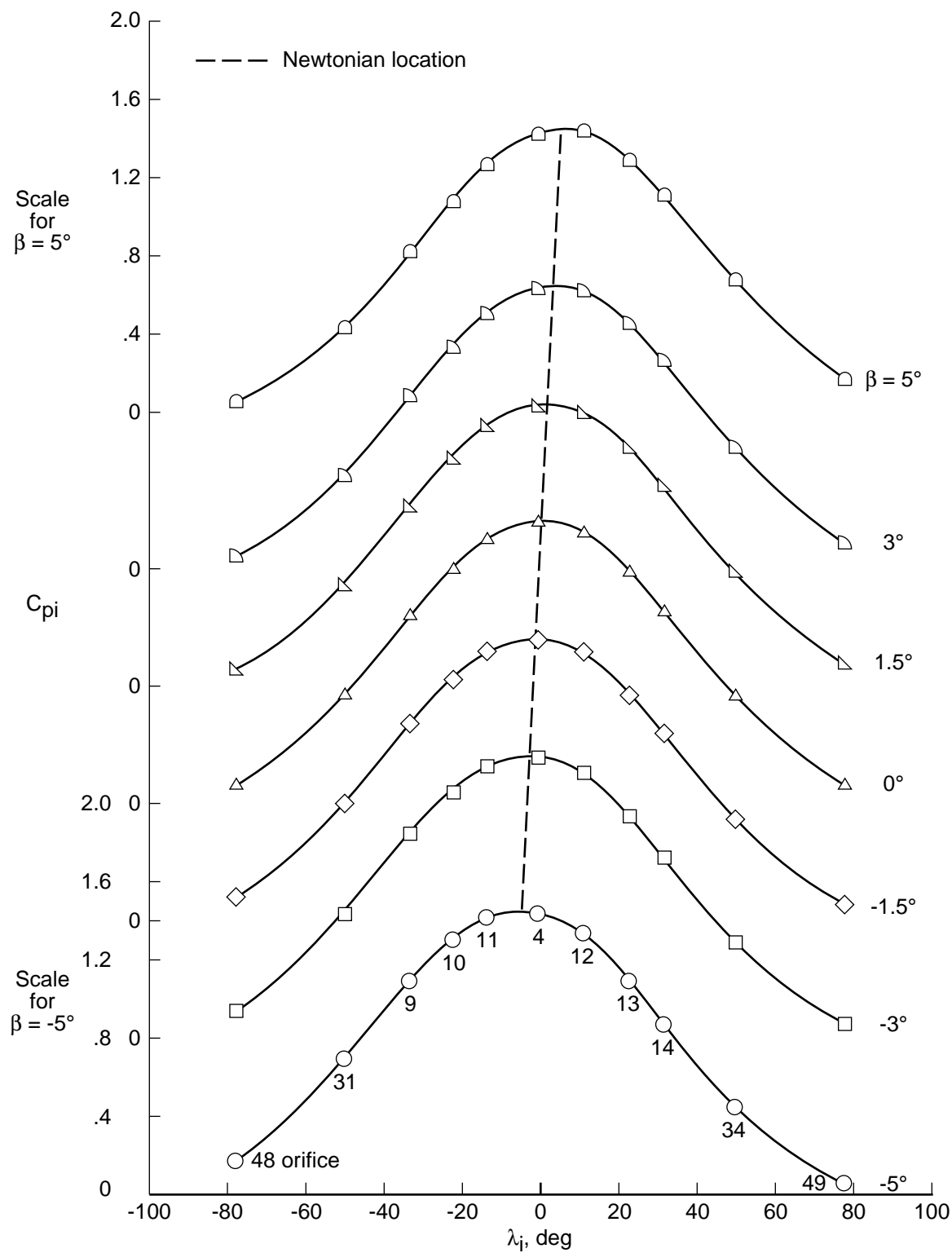


(a) $\alpha = 5^\circ$.

Figure 8. Effect of sideslip angle on pressure distributions versus lateral surface slope at constant α . $M_\infty = 21.5$.

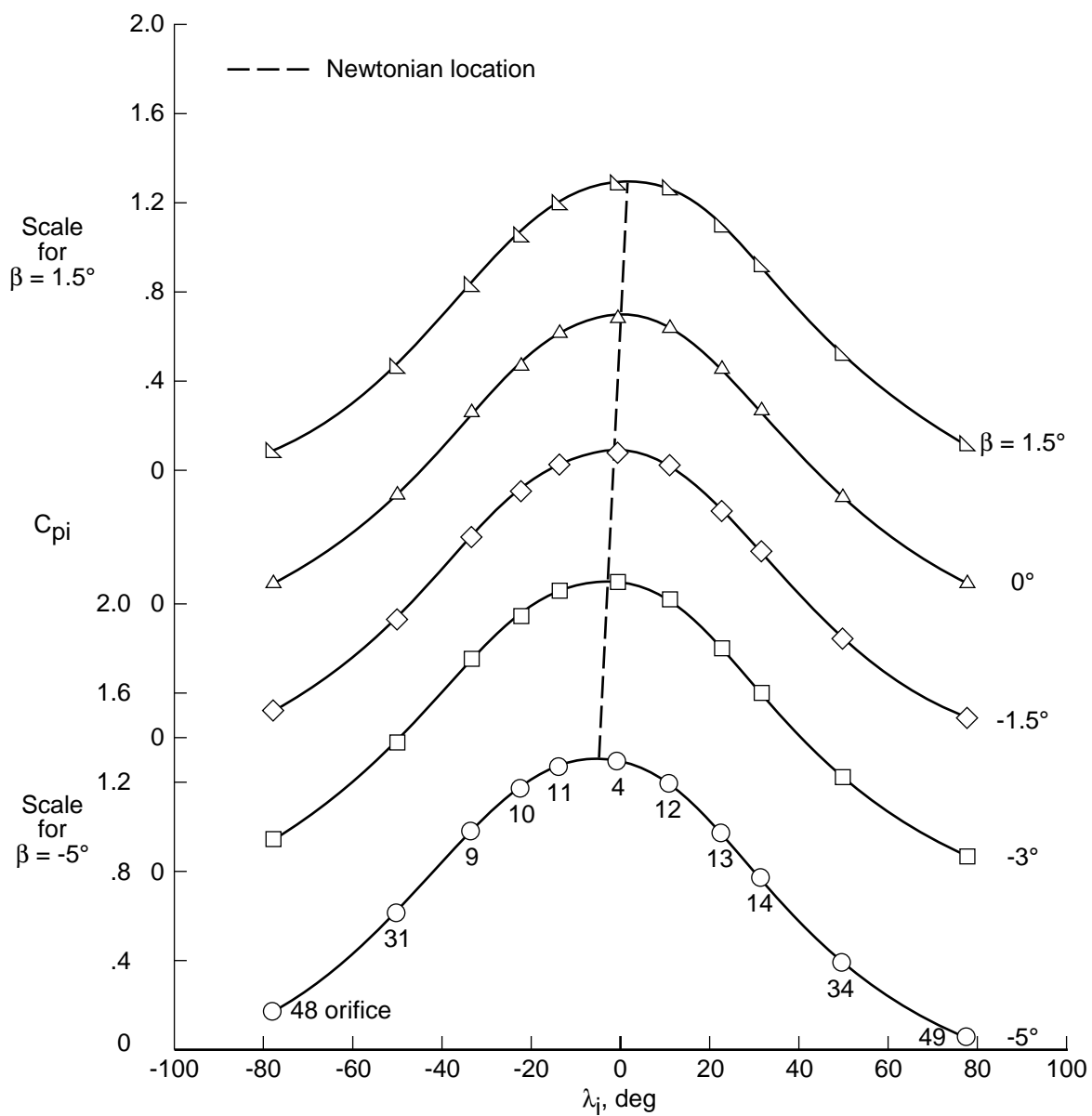


(b) $\alpha = 20^\circ$.
Figure 8. Continued.



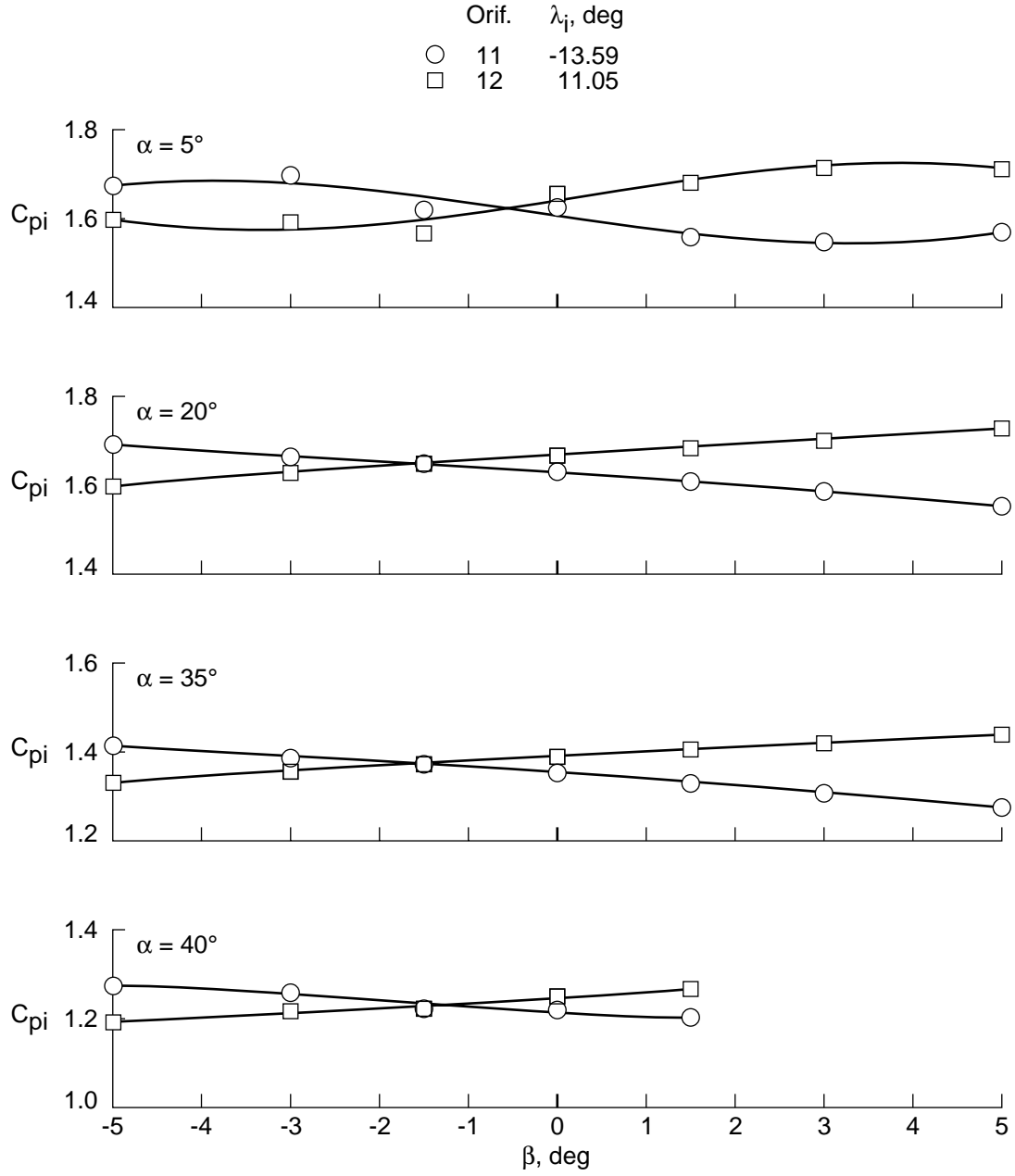
(c) $\alpha = 35^\circ$.

Figure 8. Continued.



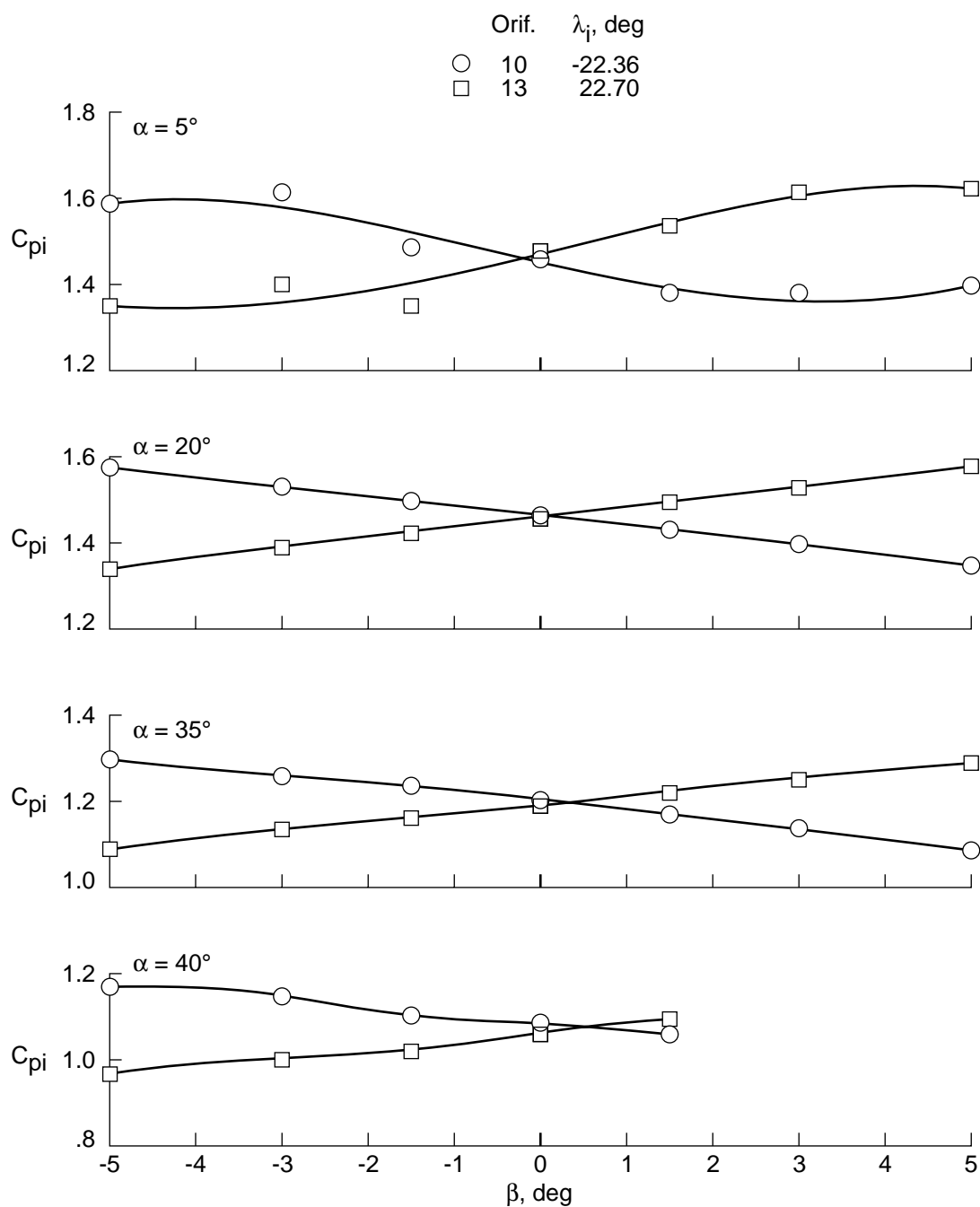
(d) $\alpha = 40^\circ$.

Figure 8. Concluded.



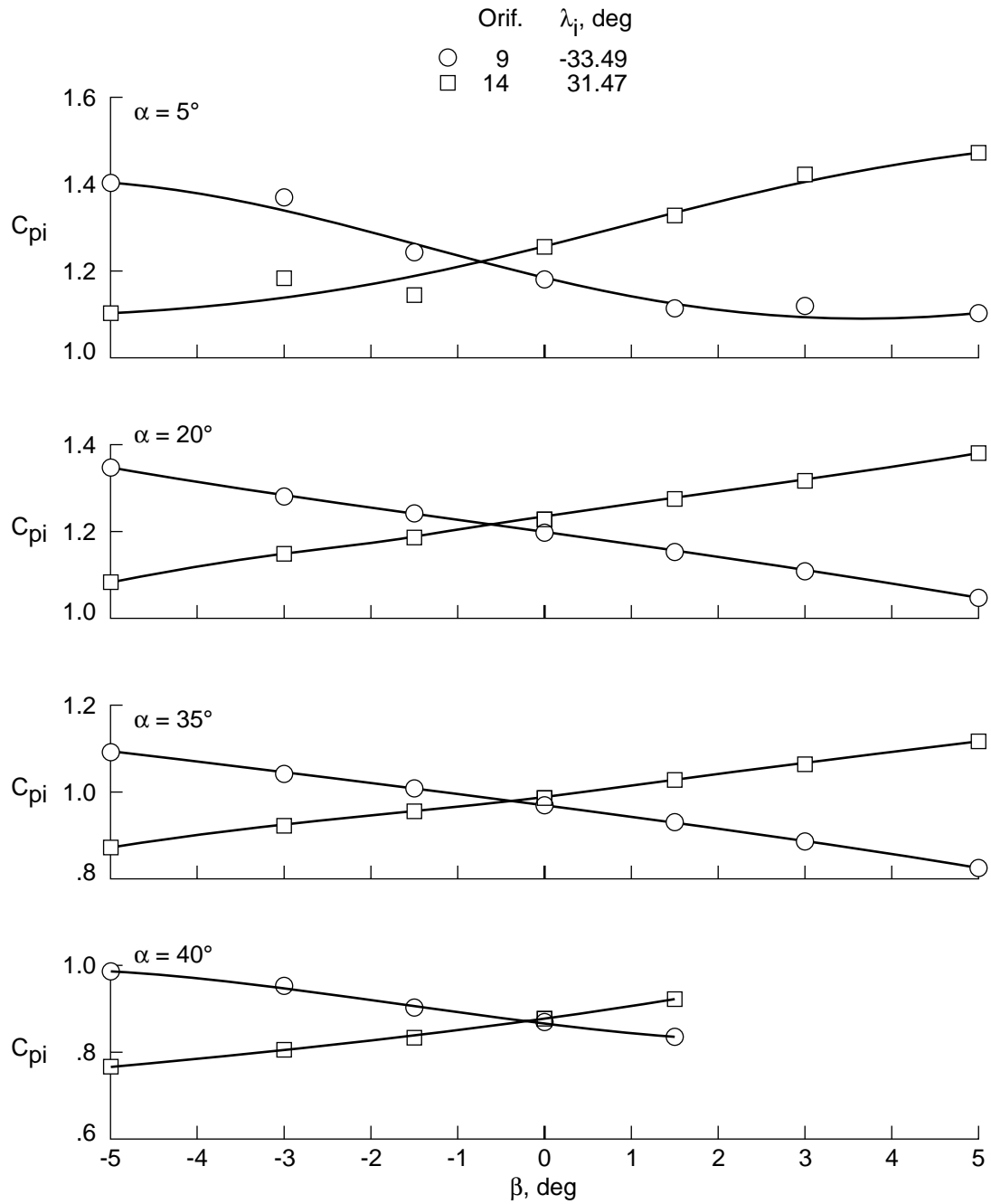
(a) Average $\lambda_i = 12.32^\circ$; $\Delta\lambda_i = -2.54^\circ$.

Figure 9. Null sideslip angle versus difference in lateral surface slope angle for matching pairs of lateral orifices at several α 's. $M_\infty = 21.5$.



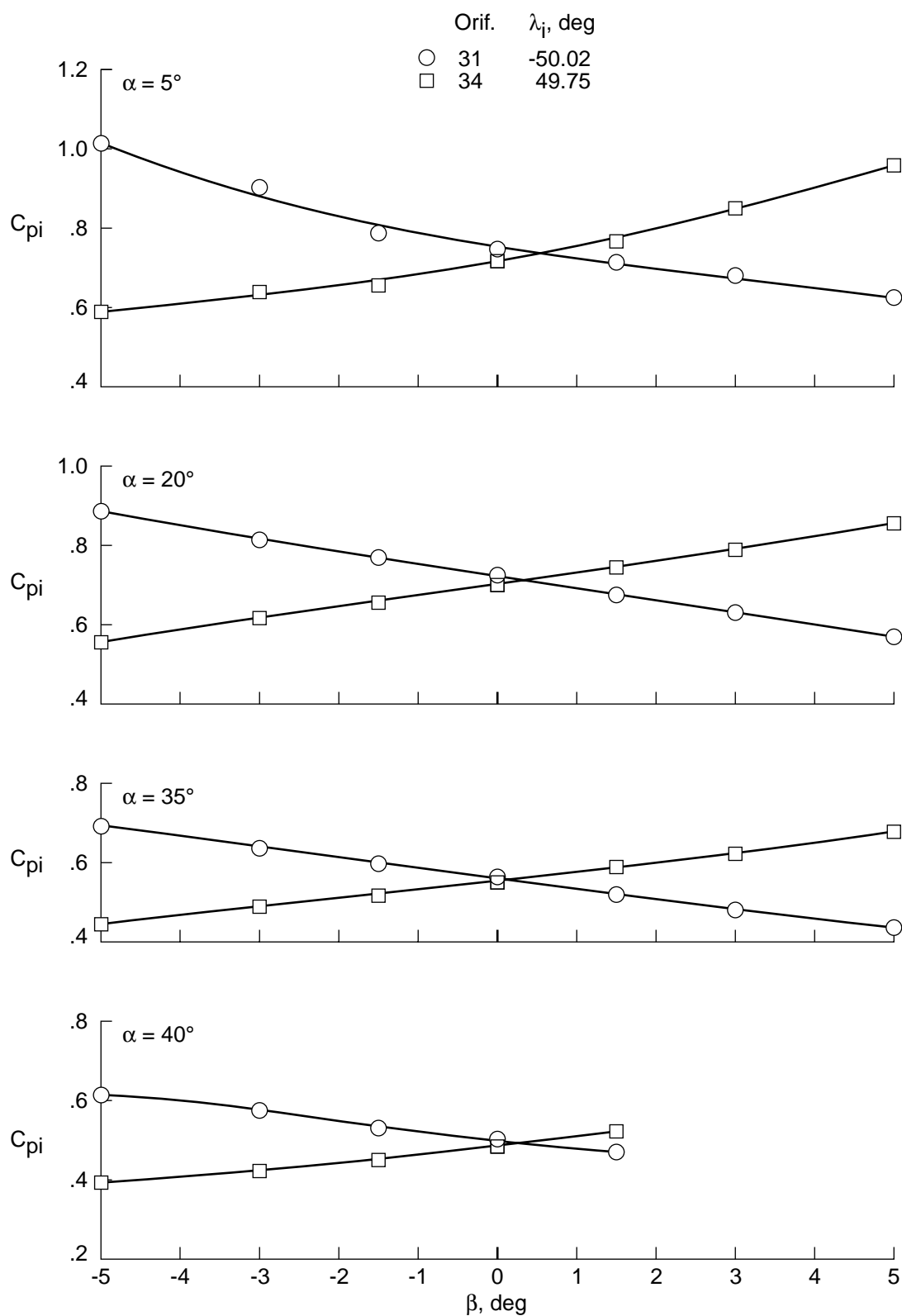
(b) Average $\lambda_i = 22.53^\circ$; $\Delta\lambda_i = 0.34^\circ$.

Figure 9. Continued.



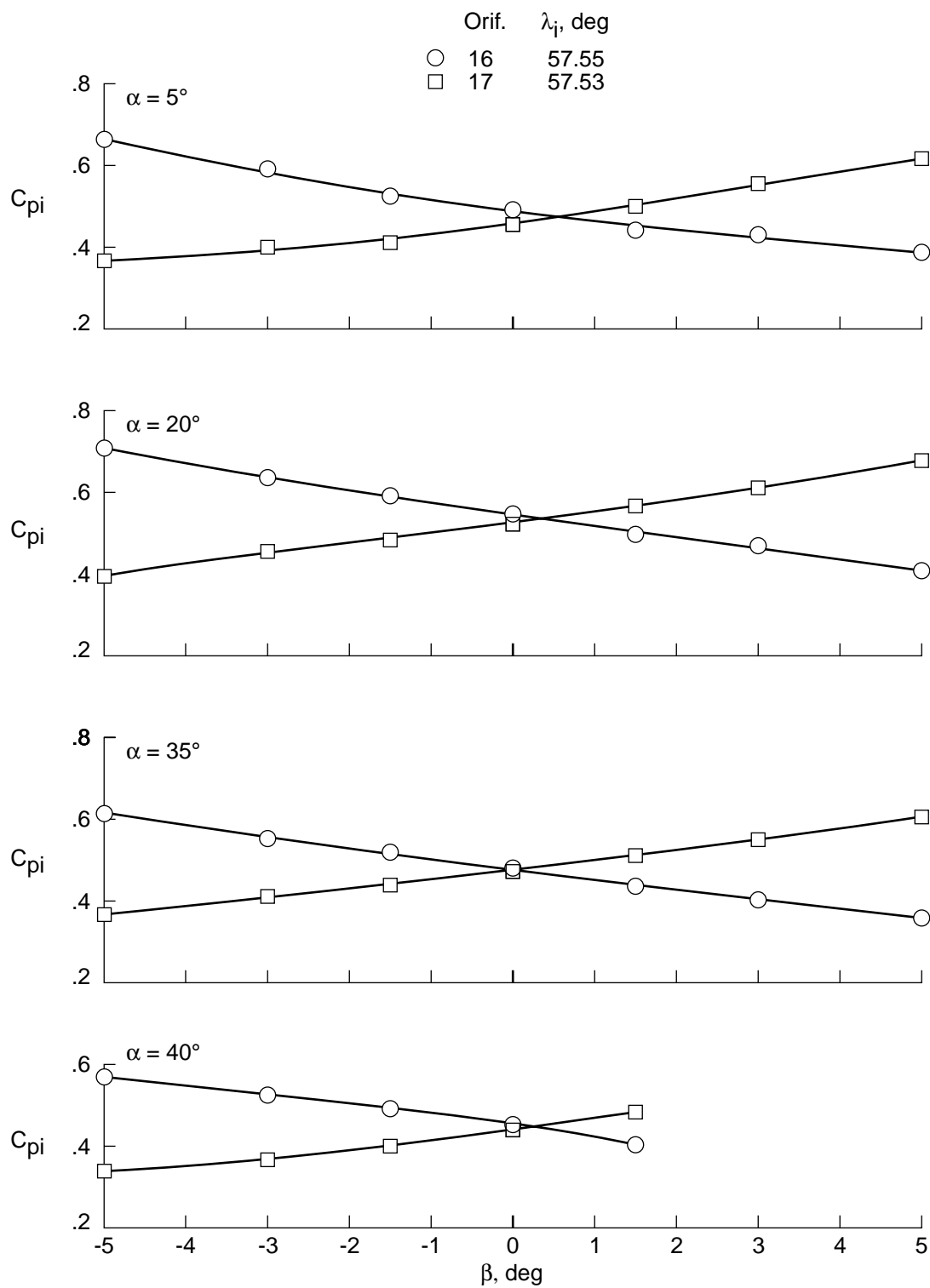
(c) Average $\lambda_i = 32.48^\circ$; $\Delta\lambda_i = -2.03^\circ$.

Figure 9. Continued.



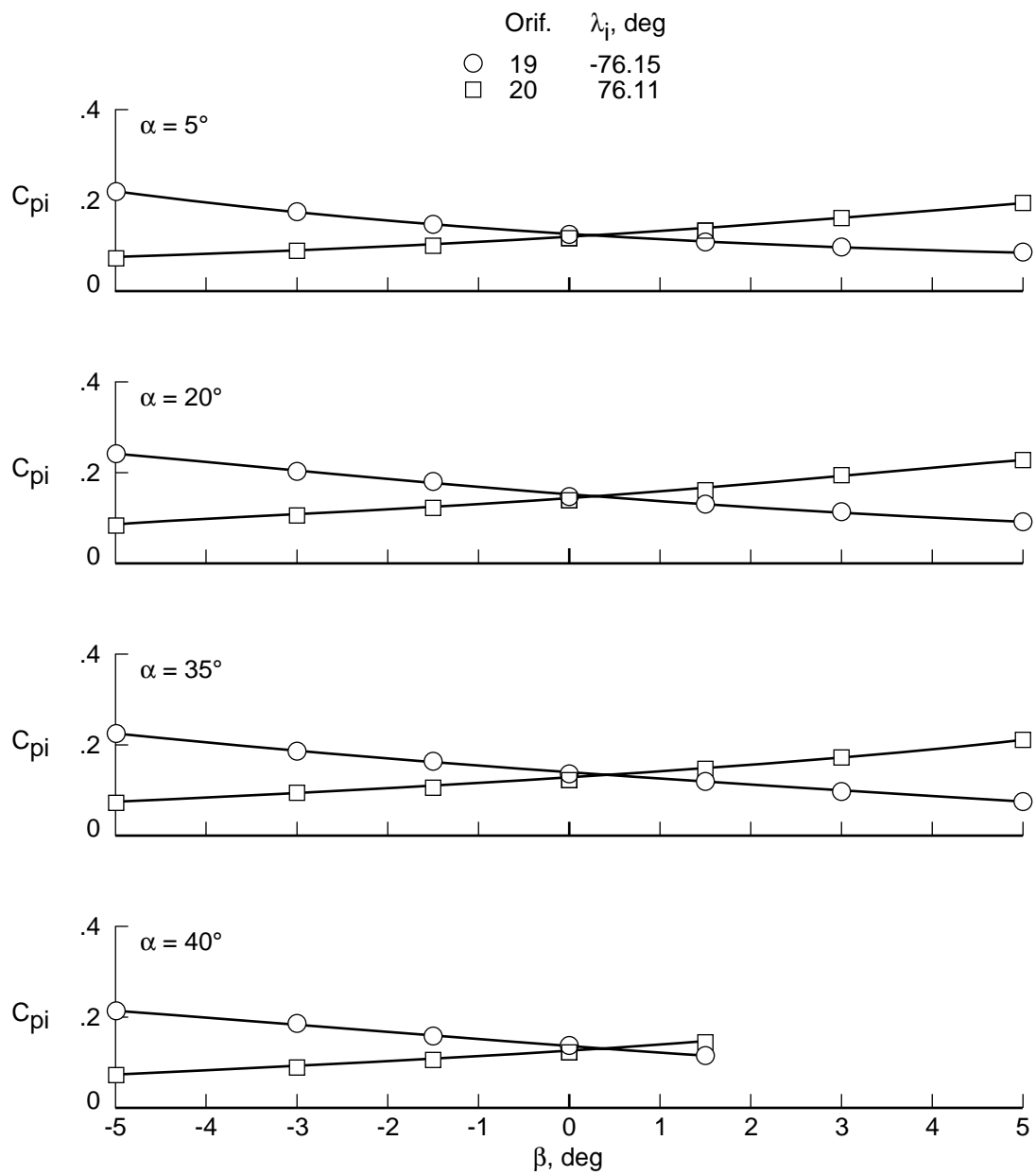
(d) Average $\lambda_i = 49.88^\circ$; $\Delta\lambda_i = -0.27^\circ$.

Figure 9. Continued.



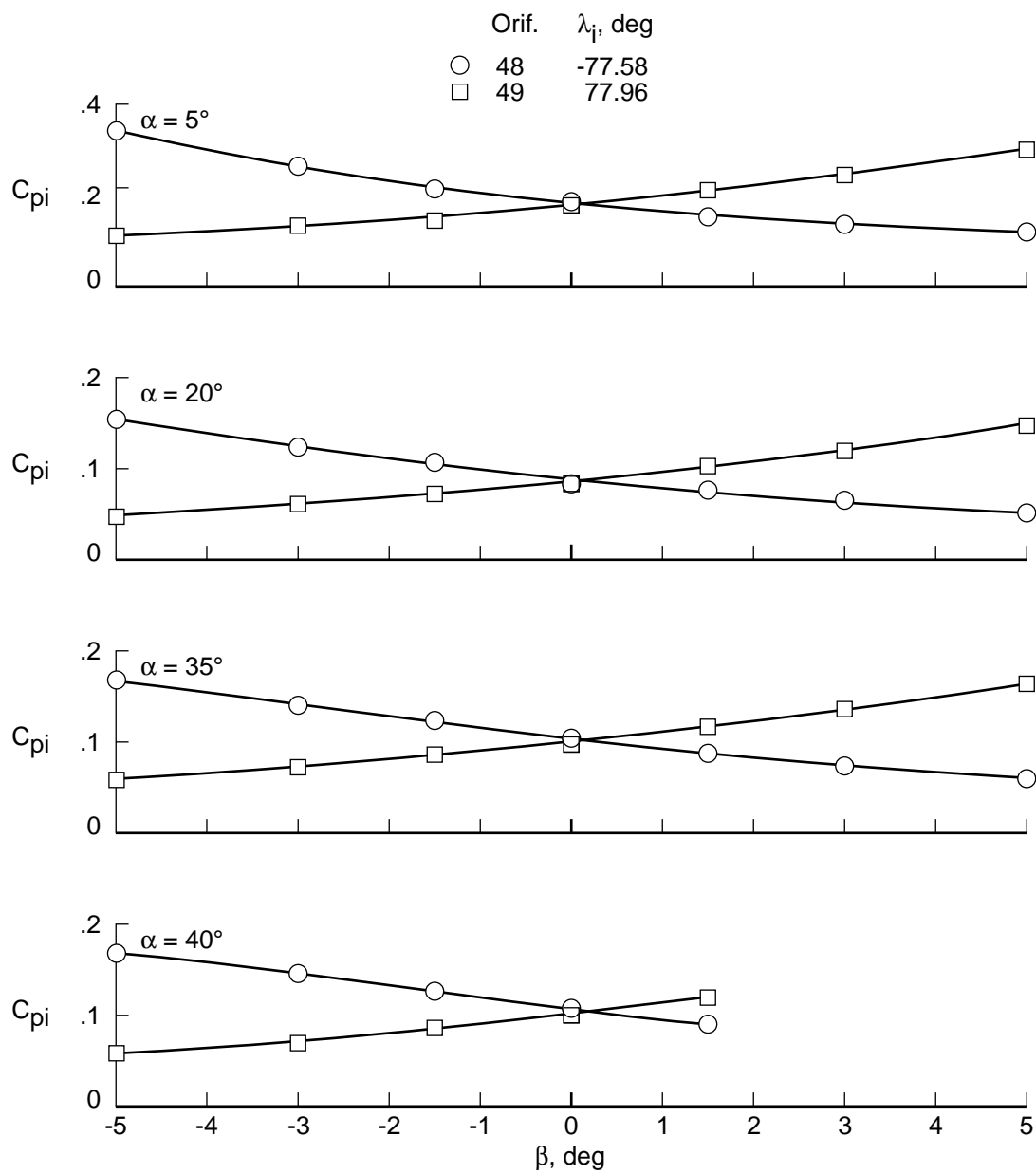
(e) Average $\lambda_i = 57.54^\circ$; $\Delta\lambda_i = -0.02^\circ$.

Figure 9. Continued.



(f) Average $\lambda_i = 76.13^\circ$; $\Delta\lambda_i = 0.03^\circ$.

Figure 9. Continued.



(g) Average $\lambda_i = 77.77^\circ$; $\Delta\lambda_i = 0.38^\circ$.

Figure 9. Concluded.

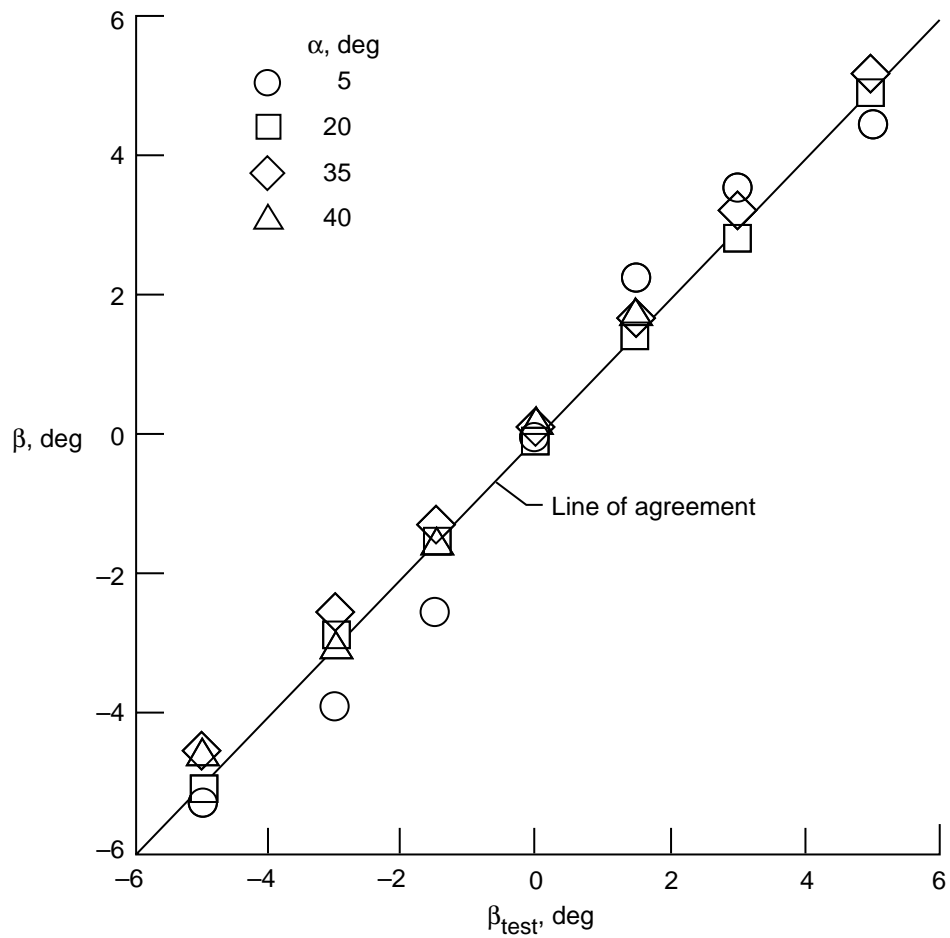


Figure 10. Model β 's set during tests versus predictions by the SEADS algorithm and pressure distributions of these tests.

(a) Front.

L-93-25

(b) Side.

Figure 1. Model and stings.

L-93-26

(a) $\alpha = 5^\circ$.

Figure 4. Electron-beam illuminated flow fields on SEADS model at several α 's.

L-93-27

L-93-28

(b) $\alpha = 25^\circ$.

Figure 4. Continued.

L-93-29

(c) $\alpha = 35^\circ$.

Figure 4. Continued.

L-93-30

(d) $\alpha = 40^\circ$.

Figure 4. Continued.

L-93-31

(e) $\alpha = 45^\circ$.

Figure 4. Continued.

L-93-32

(f) $\alpha = 50^\circ$.

Figure 4. Concluded.

REPORT DOCUMENTATION PAGE			Form Approved OMB No. 0704-0188	
Public reporting burden for this collection of information is estimated to average 1 hour per response, including the time for reviewing instructions, searching existing data sources, gathering and maintaining the data needed, and completing and reviewing the collection of information. Send comments regarding this burden estimate or any other aspect of this collection of information, including suggestions for reducing this burden, to Washington Headquarters Services, Directorate for Information Operations and Reports, 1215 Jefferson Davis Highway, Suite 1204, Arlington, VA 22202-4302, and to the Office of Management and Budget, Paperwork Reduction Project (0704-0188), Washington, DC 20503.				
1. AGENCY USE ONLY (Leave blank)		2. REPORT DATE January 1994	3. REPORT TYPE AND DATES COVERED Technical Memorandum	
4. TITLE AND SUBTITLE Pressure Distributions on a 0.02-Scale Space Shuttle Orbiter Nose at Mach 21.5 in Helium			5. FUNDING NUMBERS WU 506-40-41-01	
6. AUTHOR(S) George C. Ashby, Jr., Peter T. Bernot, and William C. Woods				
7. PERFORMING ORGANIZATION NAME(S) AND ADDRESS(ES) NASA Langley Research Center Hampton, VA 23681-0001			8. PERFORMING ORGANIZATION REPORT NUMBER L-17038	
9. SPONSORING/MONITORING AGENCY NAME(S) AND ADDRESS(ES) National Aeronautics and Space Administration Washington, DC 20546-0001			10. SPONSORING/MONITORING AGENCY REPORT NUMBER NASA TM-4495	
11. SUPPLEMENTARY NOTES				
12a. DISTRIBUTION/AVAILABILITY STATEMENT Unclassified-Unlimited Subject Category 02			12b. DISTRIBUTION CODE	
13. ABSTRACT (Maximum 200 words) Pressure distributions on a 0.02-scale model of the Space Shuttle orbiter forward fuselage were obtained in the 22-inch aerodynamic leg of the Langley Hypersonic Helium Tunnel Facility at a nominal free-stream Mach number of 21.5 and a ratio of specific heats of 1.67 for inclusion in the database of the Shuttle entry air data system (SEADS). The data were measured at model angles of attack of 0° to 50° in 5° increments for zero sideslip angle and at model sideslip angles of -5° to 5° for angles of attack equal to 5°, 20°, 35°, and 40°. These data displayed trends similar to those observed in other wind tunnels at Mach 6 and 10 in air. Specifically noted is a shift in the location of the stagnation point at angles of attack above 15°; this effect did not, however, occur in flight. By comparison, the data obtained at Mach 6 in the Langley Hypersonic CF ₄ Tunnel, corresponding to a lower ratio of specific heats in the postshock region than those in helium and air, showed some reduction of the stagnation point shift at the higher angles of attack. The differences between flight and wind tunnel pressure distributions are believed due primarily to high-temperature gas chemistry effects in flight, which include lower effective specific heat ratios but which were not completely duplicated in the wind tunnels.				
14. SUBJECT TERMS Shuttle; Pressure distributions; Real-gas simulation; Hypersonic			15. NUMBER OF PAGES 74	
			16. PRICE CODE A04	
17. SECURITY CLASSIFICATION OF REPORT Unclassified	18. SECURITY CLASSIFICATION OF THIS PAGE Unclassified	19. SECURITY CLASSIFICATION OF ABSTRACT	20. LIMITATION OF ABSTRACT	